



저작자표시-비영리-변경금지 2.0 대한민국

이용자는 아래의 조건을 따르는 경우에 한하여 자유롭게

- 이 저작물을 복제, 배포, 전송, 전시, 공연 및 방송할 수 있습니다.

다음과 같은 조건을 따라야 합니다:



저작자표시. 귀하는 원저작자를 표시하여야 합니다.



비영리. 귀하는 이 저작물을 영리 목적으로 이용할 수 없습니다.



변경금지. 귀하는 이 저작물을 개작, 변형 또는 가공할 수 없습니다.

- 귀하는, 이 저작물의 재이용이나 배포의 경우, 이 저작물에 적용된 이용허락조건을 명확하게 나타내어야 합니다.
- 저작권자로부터 별도의 허가를 받으면 이러한 조건들은 적용되지 않습니다.

저작권법에 따른 이용자의 권리는 위의 내용에 의하여 영향을 받지 않습니다.

이것은 [이용허락규약\(Legal Code\)](#)을 이해하기 쉽게 요약한 것입니다.

[Disclaimer](#)

이학박사 학위논문

Characteristics of generation and
propagation of nonlinear internal
waves observed in the northern
East China Sea

동중국해 북부해역에서 관측된 비선형 단주기
내부파의 생성 및 전파 특성

2022년 2월

서울대학교 대학원

지구환경과학부

이 승 우

A Dissertation for the degree of Ph.D.

Characteristics of generation and
propagation of nonlinear internal
waves observed in the northern
East China Sea

February 2022

School of Earth and Environmental Sciences

The Graduate School

Seoul National University

Seung-Woo Lee

Characteristics of generation and propagation of nonlinear internal waves observed in the northern East China Sea

지도교수 남 성 현

이 논문을 이학박사 학위논문으로 제출함
2022년 2월

서울대학교 대학원
지구환경과학부
이 승 우

이승우의 이학박사 학위논문을 인준함
2022년 2월

위 원 장 조 양 기 (인)

부위원장 남 성 현 (인)

위 원 나 한 나 (인)

위 원 최 우 영 (인)

위 원 변 상 신 (인)

Abstract

Characteristics of generation and propagation of nonlinear internal waves observed in the northern East China Sea

Seung–Woo Lee

School of Earth and Environmental Sciences

The Graduate School

Seoul National University

Oceanic nonlinear internal waves (NLIWs), which are closer to the period of buoyancy frequency than the period of inertial frequency, are ubiquitous in the stratified ocean, and play an important role in the transport and redistribution of heat, energy, and matter. Turbulent mixing and changes in water structure caused by NLIWs have a profound effect on marine ecosystem disturbance, fishery formation, and refraction/reflection/scattering of underwater acoustic signals. In order to understand the NLIWs and their effects, it is necessary to observe the NLIWs and understand their characteristics of wave property, generation, and propagation. In this study, I propose to develop methods of estimating the propagation speed and direction of NLIWs, to characterize of NLIWs observed from moored and underway observation in the northern East China Sea (ECS) during spring 2015, and to discuss their generation and propagation.

Propagation speed and direction of NLIWs are important parameters for

understanding the generation and propagation of waves, and ultimately clarifying regional ocean circulation. However, these parameters cannot be directly measured from in-situ instruments, but can only be estimated from post-processing in situ data. This study is suggested two methods and an optimal approach to estimate the propagation speed and direction of waves using underway and moored observations. The Doppler shift method estimates these parameters from apparent observations concerning a moving ship using the Doppler shift induced by the changing relative distance of the NLIWs from the moving ship. The time lag method estimates the parameters using the distance between two locations of the NLIW observed at different times and the time lag. To optimize the speed and direction of NLIWs, the difference in the propagation direction independently estimated by the two methods needs to be minimized concerning the optimal propagation speed to yield the optimal propagation direction. The methods were applied to two cases observed in the northern East China Sea in May 2015 and August 2018. The results derived from the proposed method are robust, as the range of propagation speeds is comparable to the interannual variation of theoretical propagation speeds estimated using historical hydrographic data, yielding an error of less than 15% for the propagation direction. Because in situ observations of NLIWs are still challenging to collect and propagation speed and direction cannot be directly measured from subsurface instruments, the proposed method for estimating the propagation speed and direction of NLIWs using common underway and moored measurements is of practical importance, particularly over a broad shelf, such as the northern ECS, where the multi-directional propagation of multi-mode NLIWs from multiple sources is often observed.

NLIWs play an important role in regional circulation, marine biogeochemistry,

energetics, underwater acoustics, among others; yet our understanding on their characteristics, generation, and propagation are still far from complete in many seas, in particular ECS. This study is presented characteristics of NLIWs observed from moored and underway observations in the northern East China Sea during spring 2015, and discussed their generation and propagation. The NLIWs observed during the experiment are characterized with an amplitude ranging from 4 to 16 m, characteristic width ranging from 380 to 600 m, which propagated southwestward with a speed of 0.64–0.72 m/s. Groups of NLIWs were dominantly observed during or a couple of days after the period of spring tides with a time interval 24–96 minutes shorter than the canonical semidiurnal period (12.42 h; M₂) in contrast to those found in many other regions with a phase locking to the barotropic semidiurnal tides. The remote generation and propagation of the mode-1 NLIWs from potential generation sites into the experimental area under time-varying stratification support the time interval departed from the semidiurnal period. The results have substantial implications for turbulent mixing and regional circulation in regions where the shelf is broad and shallow. The NLIWs generated from multiple sources propagate in multiple directions and experience time-varying stratification

Keyword: Nonlinear internal wave, underway observation, moored observation, propagation speed; propagation direction; generation; propagation; stratification; northern East China Sea

Student Number: 2016-24798

Table of Contents

Abstract	i
Table of Contents	iv
List of Figures	v
List of Tables	xiii
1. Introduction	1
1.1. Background.....	1
1.2. Nonlinear internal waves in East China Sea	5
1.3. Purpose of study.....	9
2. Data and Methods.....	10
2.1. Data and processing	10
2.2. Two models and applications	22
2.2.1. Two-layered KdV (Korteweg-de Vries) models	22
2.2.2. Empirical model	25
2.3. Estimation of propagation speed and direction.....	27
2.3.1. Estimation using moored and underway measurements	27
2.3.1.1. Doppler Shift method.....	27
2.3.1.2. Time lag method	30
2.3.1.3. Optimal propagation direction and successive propagation speed	31
2.3.1.4. Estimation of propagation direction using satellite	32
2.3.2. Applications	34
2.3.2.1. SAVEX15.....	34
2.3.2.2. IORS18	40
2.3.3. Assessment.....	45
2.3.3.1. Propagation speed	45
2.3.3.2. Propagation direction.....	48
3. Results and Discussion	49
3.1. Characteristics of NLIWs in the northern ECS.....	49

3.1.1. Observed NLIWs	49
3.1.2. Modeled NLIWs	60
3.1.3. Seasonal variation	63
3.2. Generation of NLIWs in the northern ECS	70
3.3. Propagation of NLIWs from the generation sites	75
3.4. Limitation of KdV models	78
4. Conclusion	82
References.....	85
Abstract in Korean	92

List of Figures

Figure 1.1. Global distribution of internal solitary waves. Internal waves observed from August 2002 through May 2004 (modified Jackson (2007) and Boegman and Stastna (2019)).	2
Figure 1.2. Seven previous NLIWs observations in ECS denoted dashed line and this study area.	6
Figure 1.3. Spatial distribution of internal waves from satellite images in (top) the East China Sea and (bottom) Yellow sea and East Sea (Alpers et al., 2005).	8
Figure 2.1. Zoomed-in map of the study area where the SAVEX15 was conducted (red box in Figure 1.2). Locations of UCTD and CTD data collection are marked by blue dots and orange circles, respectively. The locations of five stations (STA01–STA05), including those of two vertical line arrays (VLAs at STA02 and STA04), are marked by squares and triangles. Water depth in meter is noted with gray background contours.	11
Figure 2.2. Temperature and conductivity fitting (solid black lines) of upper (red) and lower (blue) layer of minimum temperature depths. The regressions is calculated by binned data in 0.2 °C intervals (square markers).	14
Figure 2.3. (a-c) The original and fitted vertical profiles of conductivity, salinity, and density. (d-f) The difference, mean, and one standard deviation between original and fitted vertical profiles of conductivity, salinity, and density.	15
Figure 2.4. (a) Map showing the geographic region of this study for two areas of experiments (black dashed boxes), bathymetry (grey lines), and distribution of surface manifestation of NLIWs described by Alpers et al., 2006 (blue lines) and Nam et al., 2018 (green lines). Two stations conducting historical hydrographic data sampling for the National Institute of Fisheries Science (NIFS) used in this study are marked by red open circles. Zoomed-in maps of the two areas of (b) Shallow-water Acoustic Variability EXperiment 2015 (SAVEX15) and (c) Jeodo Ocean Research Station 2018 (IORS18). Locations of underway conductivity–temperature–depth (UCTD) data collection, moored observations (VLA1 and VLA2),	

and Ieodo Ocean Research Station (IORS) are marked by blue open squares in (b,c), purple triangles in (b), and yellow stars in (c). 17

Figure 2.5. Availability map of NIFS/KODC hydrographic data in month and year between 1980 and 2019. 19

Figure 2.6. Propagation speed of nonlinear internal waves as function of water depth in northern East China Sea. The blue circles mean propagation speed of NLIW in May obtained from NIFS data, which is calculated two-layered KdV model at an amplitude of 6 m. The blue and cyan line mean the propagation speed of May climatology and May 2015, respectively. The solid black line means the empirical model from Jackson (2009), and dashed and dotted line mean modified A parameters of the empirical model to applicate in this study. 26

Figure 2.7. Schematic description of (a) the definition of parameters and estimation of the NLIW propagating direction based on the (b) Doppler shift and (c) time lag. 29

Figure 2.8. (a,b) Two satellite images where (c,d) surface manifestations of NLIWs (orange lines) are confirmed, from MODIS Terra at 02:50 UTC on 02 August 2015, and MODIS Aqua at 04:44 UTC on 30 July 2018. The blue box is the example of the propagation direction calculation. The SAVEX15 and IORS are marked by a red box and yellow star, respectively. 33

Figure 2.9. Time-depth pattern of water temperature observed from (a) northern mooring (VLA1) and (b) UCTD during the SAVEX15. The contour interval is 0.5 °C. The 13 °C isotherm is denoted by a thick black line. The times of NLIW observations at the VLA1 and UCTD are denoted by vertical grey and red dashed lines, respectively. Depths of thermistors attached to the VLA1 are denoted by black squares on the left axes. 37

Figure 2.10. (a) Time-series of 13 °C isotherm depth observed at the VLA1 (red) and UCTD (blue), and (b) vertical profiles of density obtained from the UCTD measurements (grey) at 15:10–16:14 UTC on 23 May 2015. In (b), the average profile is marked in blue, and minimum and maximum densities at the upper and lower layers (corresponding to ρ_1 and ρ_2), respectively, are shown with red dashed lines. 38

Figure 2.11. Propagation direction of NLIW observed during the SAVEX15,

estimated from (a) Doppler shift method and (b) time lag method. The ϕ_{sh} , ϕ_{obs} , θ_{ds} , and θ_{tl} are labelled in the plots. Date and times of the corresponding events are noted in the right bottom corner.39

Figure 2.12. Time-depth pattern of water temperature observed at the (a) IORS and (b) UCTD during IORS18. The contour interval is 2 °C. The 18 °C isotherm is denoted by a thick black line. Time of NLIW observations at the IORS and UCTD are denoted by vertical grey and red dashed lines, respectively. Depths of thermistors attached to the IORS are denoted by black squares on the left axes.42

Figure 2.13. Information related to NLIWs observed at the IORS and UCTD during IORS18. (a) Time-series of the depth of the 18 °C isotherm observed at the IORS (red) and UCTD (blue), and (b) vertical profiles of density obtained from the UCTD measurements (grey) at 11:02–11:59 UTC on 30 August 2018. In (b), the average profile is marked in blue, and minimum and maximum densities at the upper and lower layers (corresponding to ρ_1 and ρ_2), respectively, are shown with red dashed lines.43

Figure 2.14. Propagation direction of NLIW observed during IORS18, estimated from (a) Doppler shift method and (b) time lag method. The ϕ_{sh} , ϕ_{obs} , θ_{ds} , and θ_{tl} are labeled in the plots. Dates and times of the corresponding events are noted in the right bottom corner.44

Figure 2.15. (a) Time series of propagation speed estimated from the method proposed in this study (colored squares; red for SAVEX15 and blue for IORS18) and KdV theory (open squares, open circles, and colored lines). KdV theory was applied using the NIFS historical hydrographic data for May (red line and open circle) and August (blue line and open circle), and hydrographic data obtained during SAVEX15 and IORS18 (open squares). The propagation speed of NLIWs observed in the northern ECS in August 2005 (Lee et al., 2006) is denoted by a blue diamond. Time series of (b) thickness (h_1 and h_2) and (c) density (ρ_1 and ρ_2) of the upper (solid lines) and lower (dashed lines) layers derived from the NIFS historical hydrographic data for May (red) and August (blue), and hydrographic data obtained during SAVEX15 and IORS18 (open squares and circles for upper

and lower layers, respectively). Long-term trends of (a) propagation speed, (b) layer thickness, and (c) layer density from 1994 to 2019 are remarked with dotted lines.47

Figure 3.1. Time–depth contours of water temperature observed from VLA1 (left) and VLA2 (right) during SAVEX15. The time is separated by double M2 tidal periods (2 times 12.42 h) as indicated by the x-axes at the bottom. Timings of the NLIWs observed from the VLAs and UCTD are shown with thick black tick markers on the top x-axis and green vertical lines (labeled E1, E2, and E3), respectively.50

Figure 3.2. Cross-sectional structures of water temperature observed from UCTD during (a) E1, (b) E2, and (c) E3. The contour interval is 0.5 °C and the 13 °C isotherms are denoted by thick black lines. Maximum and minimum isotherm depths displaced by the NLIWs are indicated with red squares and circles, respectively. Timings of the UCTD profiling are noted with thick black tick markers on the top x-axis. The NLIW events and directions of ship movement during the UCTD profiling are marked with colored lines on the bottom x-axis and black horizontal arrows, respectively. The scale bar for 1 km is shown in the bottom right corner.51

Figure 3.3. Time–depth contours of water temperature observed from (top) VLA1 and (bottom) VLA2 during the NLIWs events of (a, d) E1, (b, e) E2, and (c, f) E3. The contour interval is 0.5 °C and the 13 °C isotherms are denoted by thick black lines. Timings of the UCTD observations on NLIWs are remarked with gray vertical lines, and maximum and minimum isotherm depths observed from the UCTD (same as shown in Figure 4) displaced by the NLIWs are indicated with red squares and circles, respectively, whereas the maximum isotherm depths observed from the VLA-1 displaced by the NLIWs are indicated with red triangles in (a)–(c). White squares on the left axes denote depths of thermistors attached to the VLAs.52

Figure 3.4. Schematics showing propagation direction of NLIWs observed during the events of (a) E1, (b) E2, and (c) E3, estimated from the Doppler shift method (green arrows) and the time lag method (blue arrows) where the propagation directions used to yield the optimal propagation direction are shown with thick solid arrows (others not used are marked as thick dashed

arrows). The ϕ_{sh} , ϕ_{obs} , θ_{ds} , and θ_{tl} are labelled in the plots. Date and times of the corresponding events are noted in the bottom corners53

Figure 3.5. (a) Time series and (b) M2 tidal phase of sea level anomaly (solid black lines) observed at the IORS where timings of NLIWs observed at VLA1, VLA2, and UCTD are marked with red and blue dots and green crosses. In (a) and (b), the y-axis and radial axis represent sea level anomalies. The periods of spring and neap tides are denoted by gray and white areas, respectively, in (a). Timings of the UCTD profiling are noted with thick black tick markers on the top x-axis in (a), and total measurement periods of VLAs are denoted with a thick black horizontal line on the top x-axis.57

Figure 3.6. (a) Satellite MODIS Terra image taken in the northern ECS at 02:32 UTC on 20 July 2018 where surface manifestations of three types (Type-A; yellow, Type-B; blue, and Type-C; green) of NLIWs are identified. (b) Map of maximum depth-integrated M2 internal tide-generating body force in $m^2 s^{-2}$ derived from buoyancy frequency from the WOA18 data, where the surface patterns of three types of NLIWs propagating from three potential generation sites i), ii), and iii) are superimposed on the bathymetry (thin gray contours). Surface manifestations of (c) all (gray), (d) Type-A (yellow), (e) Type-B (blue), and (f) Type-C (green) NLIWs identified from 93 MODIS images, superimposed on bathymetry (blue colors) and wave fronts (black contours labelled with model propagation time in day) estimated using the empirical model (Jackson, 2009) with a wave speed parameter $A = 2.4 m s^{-1}$. Minimum distances between the generation sites (yellow stars) and the SAVEX15 area (red boxes) are marked with thick gray lines in (d), (e), and (f).59

Figure 3.7. Time series of hourly binned (a) upper (t_1 , solid lines) and lower (t_2 , dashed lines) layer temperatures, (b) upper (ρ_1 , solid lines) and lower (ρ_2 , dashed lines) layer densities, (c) upper (h_1 , solid lines) and lower (h_2 , dashed lines) layer thicknesses at VLA1 (red) and VLA2 (blue), and (d) propagation speed at VLA1 (red dashed line) and VLA2 (blue dashed line)..61

Figure 3.8. The propagation speeds of NLIWs are shown as functions of (a) t_1 , (b)

t_2 , and (c) temperature difference ($t_2 - t_1$), (d) ρ_1 , (e) ρ_2 , and (f) density difference ($\rho_2 - \rho_1$), and (g) h_1 , (h) h_2 , and (i) layer thick difference ($h_2 - h_1$) at VLA1 (red) and VLA2 (blue). In (d)–(l), the binned mean and one standard deviation from the mean are denoted with colored circles and vertical bars, respectively.62

Figure 3.9. (a) Characteristic width and (b) propagation speed of NLIWs as a function of the wave amplitude η_0 obtained using the two layered KdV model from the historical hydrographic NIFS data collected in May, or May climatology (black solid lines, same as presented in Cho et al., 2016) and SAVEX15 VLAs data collected in May 2015 (blue solid lines), where the standard deviations from the mean are denoted with black and blue dotted lines, respectively. Characteristic width and propagation speed of NLIWs during the events of E1, E2, and E3 obtained using the two layered KdV model from the SAVEX UCTD data (open squares) and optimal approach presented in Lee and Nam (2021) using the Doppler shift method and time lag method (filled circles) are compared.65

Figure 3.10. Propagation speed of NLIWs as function of water depth in northeastern East China Sea. The open and color markers mean propagation speed of NLIW each season from model and in-situ observation. The color solid lines mean historical climatology data, which is calculated two-layered KdV model at an amplitude of 6 m, with interval of 20 m as derived from the NIFS/KODC data (red: January, February, and March; blue: April, May, and June; yellow: July, August, and September; green: October, November, and December). The shaded area means one standard derivation. The gray dashed line means modified A parameters of empirical model (Equation 2.11).....68

Figure 3.11. Seasonal spatial map of (a, d, g) propagation speed of NLIWs, (b, e, h) difference of density between upper layer and lower layer density, and (c, f, i) difference of water thickness between upper layer and lower layer in spring (a-c), summer (d-f), and fall (g-i). The historical hydrographic data from NIFS KODC denote black cross markers. The black box denotes the SAVEX15 area.69

Figure 3.12. Water depth, tide amplitude and phase, tidal transport, bottom slope, depth-normalized buoyancy frequency, and internal tide generating body force.72

Figure 3.13. Map of maximum depth-integrated M2 internal tide-generating body force in $\text{m}^2 \text{s}^{-2}$ derived from buoyancy frequency from the WOA18 data, where the surface patterns of three types of NLIWs (i, ii, and iii) propagating from four potential generation sites (a-d). The (d) images is from Nam et al., (2018).73

Figure 3.14. Map of horizontal barotropic tidal energy flux (W m^{-1}) for M2 constituent derived from the WOA18 data in five stages (a-e).74

Figure 3.15. (a) Time series of daily binned propagation speed of NLIWs (colored squares) estimated from VLAs data with its standard deviations (vertical bars) and (b) daily profiles of propagation speed of NLIWs as a function of water depth estimated using the empirical model by fitting to the daily variations of propagation speed at VLA1. In (a), the propagation speeds in May 15–18 were obtained by linearly extrapolating the speeds in May 19 and 20. Water depth profiles along the lines (shown in Figure 3.6d, 3.6e, and 3.6f with thick gray lines) between the VLA1 and generation sites i), ii), and iii) (yellow stars) for (c) Type-A, (d) Type-B, and (e) Type-C NLIWs. Time–distance contours of propagation speed of (f) Type-A, (g) Type-B, and (h) Type-C NLIWs with labels in m s^{-1} . Timings of the arrival of observed (red, shown in Figure 3.1 left), Type-A (yellow), Type-B (blue), and Type-C (green) waves a–e in VLA1 as a function of M2 phase.77

Figure 3.16. The two case of two-layered density structure. The vertical profiles of density obtained from the UCTD measurements (grey) and the average profile (blue). The minimum and maximum densities at the upper and lower layers are shown with red dashed lines and the averaged densities at the upper and lower layers are shown with green dotted lines.80

Figure 3.17. Examples of mode-2 NLIWs observed UCTD during SAVEX15..81

List of Tables

Table 2.1. Nonlinear internal wave parameters for the two cases observed, with calculated and estimated values.	36
Table 3.1. Observed, calculated, and estimated parameters of nonlinear internal waves (NLIWs) for the three events (E1, E2, and E3).	54
Table 3.2. Applications of the two layered Korteweg-deVries (KdV) and empirical models to the northern East China Sea (ECS) for May 2015. (Top) Daily binned, propagation speed (V) at VLA1 estimated from the KdV model and wave speed parameter (A) of the empirical model. (Bottom) Differences in arrival time and corresponding M2 tidal phase of three types (Type-A, -B, and -C waves) of NLIWs at VLA1 (waves a–e), for both observed and modelled waves (generated in sites i), ii), and iii), respectively). Numbers in parentheses denote difference from the observations.	56

1. Introduction

1.1. Background

The nonlinear internal waves (NLIWs) are ubiquitous in world coastal regions and marginal seas (Figure 1.1), accompanying isopycnal fluctuations with a sharp vertical density gradient, and playing an important role in regional circulation, local biogeochemistry, energetics, vertical mixing and underwater acoustics. The NLIWs may evolve from the nonlinear steepening of internal tides generated when tidal currents flow over abrupt topography such as shelf breaks, islands and submarine ridges (Jackson et al., 2012). After generation, NLIWs often persist for a few days traveling hundreds of kilometers until they shoal into shallow water. During the shoaling stage, NLIWs can fission into multiple waves, reverse their polarity, and break, all of which induce strong and rapid turbulent dissipation and mixing (Zhao et al., 2004; Alford et al., 2015; Grimshaw et al., 2016; Bai et al., 2018). They affect transportation of momentum, heat, and energy via the turbulent energy dissipation and vertical mixing (MacKinnon and Gregg, 2003; Alford, 2003; D'Asaro et al., 2007; Moum et al., 2007; Shroyer et al., 2010; Whalen et al., 2020). Marine ecosystems are significantly influenced by the vertical nutrient supply, chlorophyll bloom, and biological redistribution which can be modulated by the NLIWs (Pineda, 1991; Scotti and Pineda, 2007; Lucas et al., 2011; Muacho et al., 2013; Villamana et al., 2017; Li et al., 2018). The NLIWs drive sediment resuspension and transportation affecting the marine geophysics and underwater acoustics (Bogucki et al., 1997; Klymak and Moum, 2003; Kuperman and Lynch, 2004; Apel et al., 2007; Boegman and Stastna., 2019).

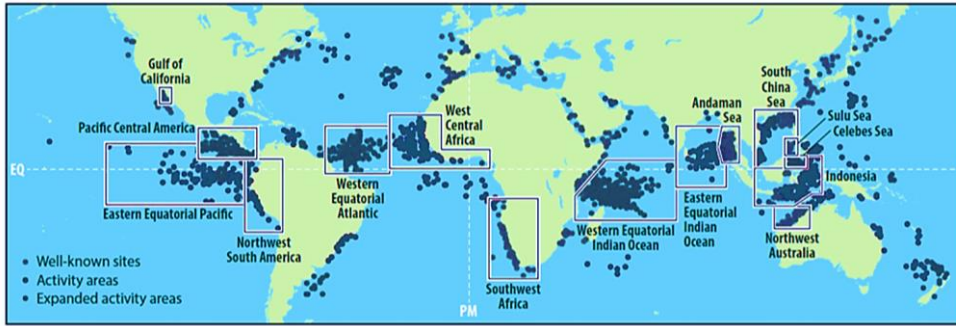


Figure 1.1. Global distribution of internal solitary waves. Internal waves observed from August 2002 through May 2004 (modified Jackson (2007) and Boegman and Stastna (2019)).

Vertical isopycnal displacements, which allow the wave amplitude to be defined, and propagation speed and direction, are fundamental parameters of NLIWs that are useful, but cannot be directly measured from in situ sampling, for a clear understanding of their generation, propagation, evolution, and dissipation. Estimating the propagation speed and direction can be important for assessing regional ocean circulation, biogeochemical cycles, energetics, underwater acoustics, and the dynamics of NLIWs.

Methods to estimate the propagation speed and direction have been suggested but are mostly limited by sampling strategies that have not yet been validated, and in-situ observations of NLIWs are still challenging to collect and propagation speed and direction cannot be directly measured from subsurface instruments. The most common method using multiple moorings aligned in the propagation direction of NLIWs aims to divide the distance between the mooring locations by the arrival time differences (Lee, 1961; Ramp et al., 2004; Moum and Nash, 2008; Shroyer et al., 2009; Alford et al., 2010). However, it is not practical to deploy many moorings along the ray of NLIWs, particularly where the continental shelf is wide and multiple NLIWs are generated from multiple sources with different unknown propagation directions.

Another method is to use the principal direction of the wave-induced horizontal velocity and the temporal difference of enhanced echo intensity from acoustic Doppler current profiler (ADCP) measurements (Scotti et al., 2005; Moum and Smyth, 2006; Mirshak and Kelley, 2009; Chang et al., 2011; Zhang et al., 2015). This method is useful, but not very practical, as extracting the propagation speed and direction is not straightforward. Using remote sensors, such as synthetic aperture radar (SAR) and spectroradiometer, the propagation speed and direction can be

estimated from the horizontal curvature of satellite images (Wang et al., 2013; Greskowiak, 2014; Lindsey et al., 2018; Karang et al., 2019; Tensubam et al., 2020); however, the limited spatiotemporal satellite sampling from polar orbits does not allow NLIWs to be easily detected. Therefore, it is necessary to develop a method to estimate the propagation speed and direction of NLIWs from widely used ship-based in situ measurements.

1.2. Nonlinear internal waves in East China Sea

In the East China Sea (ECS), NLIWs remain poorly characterized, primarily due to a lack of in-situ observation. The understanding on their generation, propagation, evolution, and dissipation is in a primitive state. During the stratified season, many NLIWs are seen in the region due to their generation by strong tides over the continental slope in the southeastern ECS or around many small islands and seamounts in the northern ECS, e.g. Ieodo Ocean Research Station (IORS, star in Figure 1.2) is based on the submerged rock 4.6 m below mean sea level. A few studies have been reported on the characteristics of ECS NLIWs from in-situ observations and satellite imagery (Figure 1.2). A packet of NLIWs with an amplitude of 2–5 m propagating northwestward at a speed of 0.6–1.1 $m s^{-1}$ was reported from in-situ observations in the northern ECS for August 2005 (Lee et al., 2006). Similar NLIWs with an amplitude of 3–5 m, a characteristic width of 200–300 m, and a propagating speed of 0.8–1.0 $m s^{-1}$ but with multiple propagating directions were observed from another field experiment conducted in August 2008 (Smith, 2010). Satellite synthetic aperture radar (SAR) images have been used to address the seasonal frequency and few distinct patterns of NLIWs in the ECS (Hsu et al., 2000; Alpers et al., 2005; Teixeira et al., 2006; Nam et al., 2018). Such characteristics of NLIWs directly estimated from in-situ and/or satellite observations are consistent with those derived from historical hydrographic data collected over 50 years based on the two-layered Korteweg-de Vries (KdV) theories (Cho et al., 2016). However, most previously reported NLIWs are limited to observation on summer season, and those in other seasons have not been investigated. In addition, the generation and propagation of NLIWs in the ECS have not yet been unraveled.

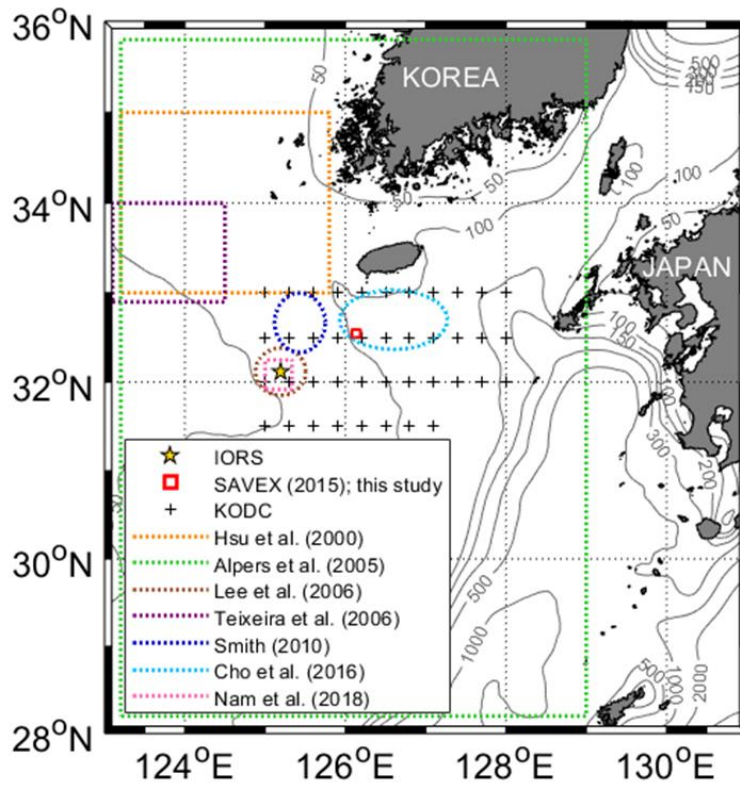


Figure 1.2. Seven previous NLIWs observations in ECS denoted dashed line and this study area.

In addition, addressing the ECS NLIWs looks more challenging than the neighboring South China Sea (SCS) and East Sea (ES) in a few aspects. Dominant originating area is the Luzon Strait for the SCS NLIWs (Zhao and Alford, 2006; Farmer et al., 2009; Guo and Chen, 2014; Wang et al., 2013; Alford et al., 2015) and continental shelf of southern Ulleung Basin for ES NLIWs (Park and Watt, 2006; Nam and Park, 2008; Jeon et al., 2014; Noh et al., 2020), in contrast ECS NLIWs have multiple (largely unknown) origins (Hsu et al., 2000). Mainly westward propagation of NLIWs from the Luzon Strait for SCS (Alpers et al., 2005; Wang et al., 2013; Ramp et al., 2010) and northward propagation of NLIWs from the southern Ulleung Basin for ES (Park and Watt, 2006; Nam and Park, 2008) are compared multiple directions of propagation from multiple sources and generations in the ECS (Hsu et al., 2000). Typically large amplitudes ($O(10^2)$ m) for SCS and $O(10)$ m for ES) with high propagation speeds $O(1)$ m/s) for SCS and ES are compared small amplitudes under 10 m with low speeds of $O(10^{-1})$ m/s) of the ECS NLIWs,

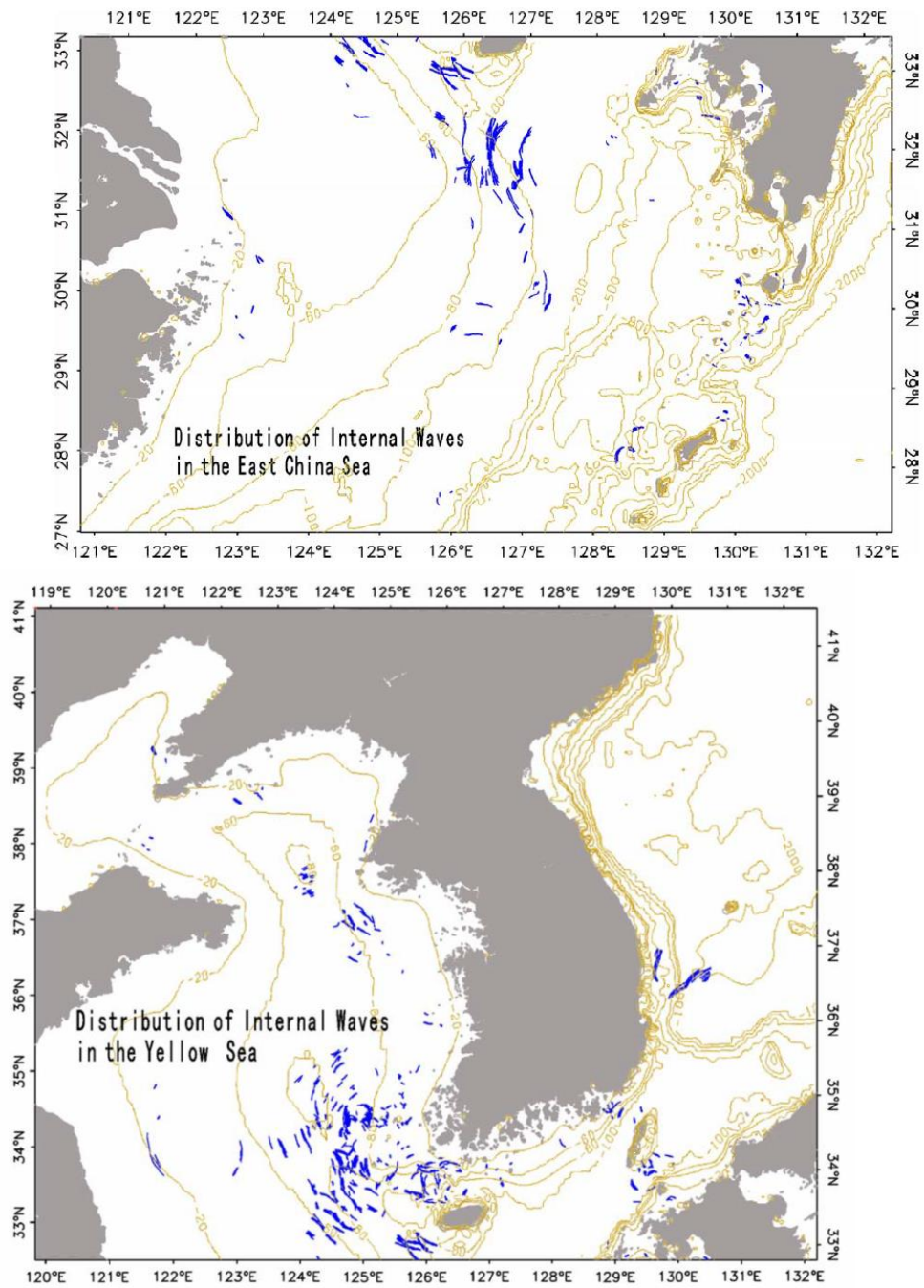


Figure 1.3. Spatial distribution of internal waves from satellite images in (top) the East China Sea and (bottom) Yellow sea and East Sea (Alpers et al., 2005).

1.3. Purpose of study

This study aims (1) to present a new method for estimating the propagation speed and direction of NLIWs using both moored and underway measurements, (2) to characterize NLIWs observed in spring (May) in the northern ECS based on in-situ observations supplemented by satellite and historical hydrographic data, and (3) to discuss the generation and propagation of mode-1 NLIWs in the region by applying KdV and empirical models.

2. Data and methods

2.1. Data and processing

Shallow-water Acoustic Variability EXperiment 2015 (SAVEX15) was conducted 14–28 May 2015 at a water depth of ~100 m (red box in Figures 1.2) in the northern ECS (Lee et al., 2020; Song et al., 2018). During the experiment, two vertical line arrays (VLAs), conductivity-temperature-depth (CTD), and underway CTD (UCTD), were used to collect moored temperature time series at multiple depths, and vertical profiles of temperature and salinity data (Figure 2.1).

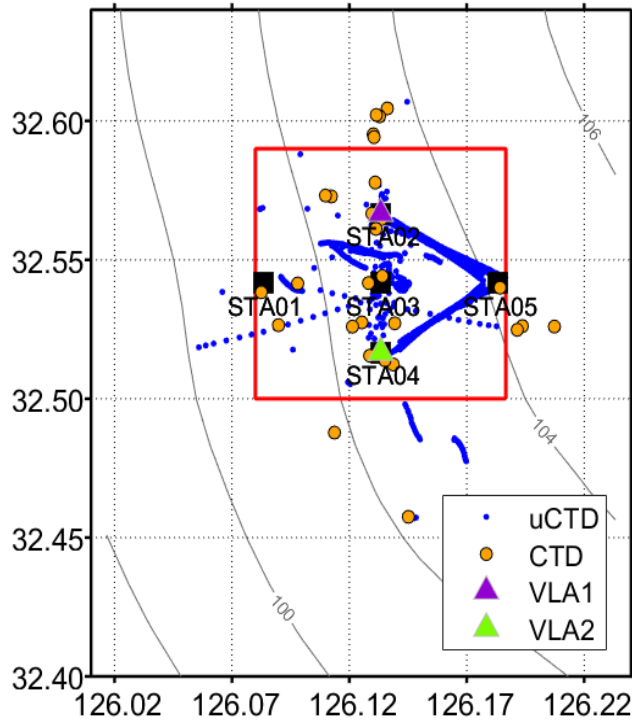


Figure 2.1. Zoomed-in map of the study area where the SAVEX15 was conducted (red box in Figure 1.2). Locations of UCTD and CTD data collection are marked by blue dots and orange circles, respectively. The locations of five stations (STA01–STA05), including those of two vertical line arrays (VLAs at STA02 and STA04), are marked by squares and triangles. Water depth in meter is noted with gray background contours.

Vertical temperature and salinity profiles were observed using the standard CTD (24-Hz Sea-Bird Electronics 911plus CTD) and UCTD (16-Hz Teledyne Oceansciences UCTD). The total number of profiles collected using the CTD and UCTD were 26 and 1,064, with typical descending speeds of less than ~ 1 and ~ 4 m s^{-1} , respectively. The CTD data were processed using standard data processing software to remove abnormal values (wild editing), correct the misalignment of temperature and conductivity sensors (align CTD), and correct the thermal inertia effect that occurs when the CTD passes by a thermocline layer (Cell TM) (Sea-Bird Electronics Inc., 2005). The UCTD data were processed following the method described by Ullman and Hebert (2014), except for the alignment process to correct the mismatch due to different response times of the conductivity and temperature sensors. The raw temperature and conductivity measured using the UCTD were filtered with a cutoff period of four scans (0.25 s). The raw pressure measured using the UCTD was filtered with a cutoff period of 32 scans (2 s). The time delay between the conductivity and temperature sensors was corrected using lagged correlation. Then, spikes in the salinity data were removed through alignment between the temperature and conductivity sensors. Finally, the data were corrected for the effect of viscous heating and averaged over a 1 dbar bin vertically.

Both VLA1 and VLA2, separated by approximately 5.5 km, where 25 temperature loggers and 5 Star-Oddi temperature-depth-tilt sensors were attached at depths ranging from 2 to 80 m, and were moored at two stations, STA02 and STA04, respectively. The sampling time interval of the moored temperature sensors was 30 s. Depths of the moored temperature sensors attached to the VLAs were corrected using the tilt and pressure data recorded by the five Star-Oddi temperature-depth-tilt sensors. After removing outliers, the moored temperature data were vertically

interpolated using the Akima spline method (Akima, 1970) with an interval of 1 m. Since no conductivity sensor was attached to VLAs, we estimated the conductivity. We calculated the salinity and density using linear relationships between temperature and conductivity derived from vertical temperature and conductivity profiles observed using the CTD and UCTD (Figures 2.2 and 2.3).

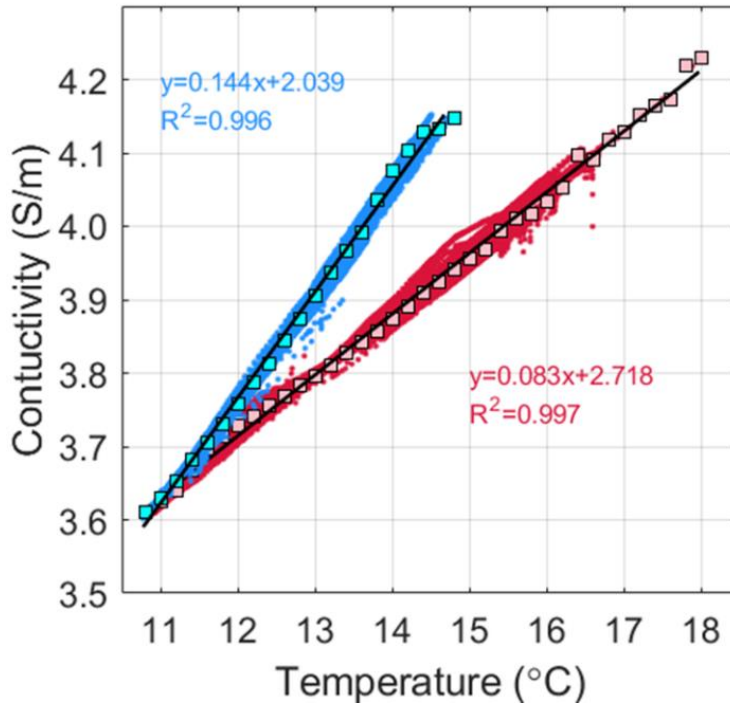


Figure 2.2. Temperature and conductivity fitting (solid black lines) of upper (red) and lower (blue) layer of minimum temperature depths. The regressions is calculated by binned data in 0.2 °C intervals (square markers).

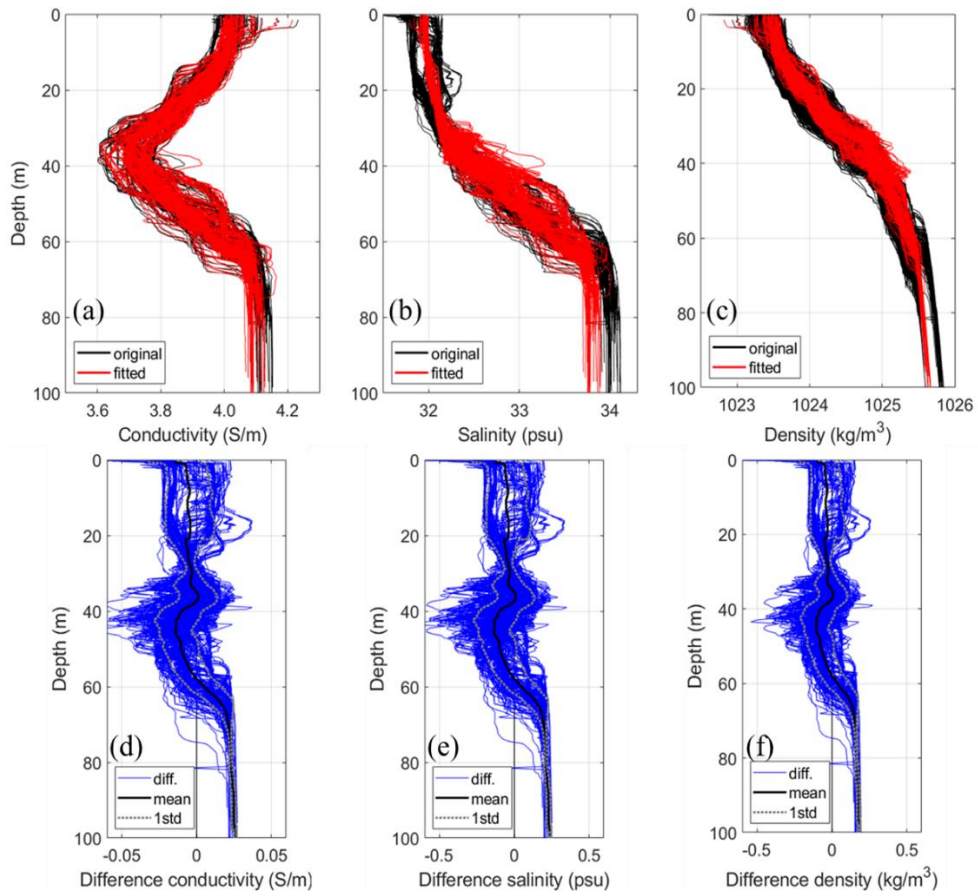


Figure 2.3. (a-c) The original and fitted vertical profiles of conductivity, salinity, and density. (d-f) The difference, mean, and one standard deviation between original and fitted vertical profiles of conductivity, salinity, and density.

Ieodo Ocean Research Station 2018 (IORS18) was conducted in the northern ECS in the vicinity of IORS (32°7.4 N, 125°10.9 E, constructed at a water depth of 41 m) on 28 August–1 September 2018 (Figure 2.4a,c). During the IORS18 experiment, UCTD was used to collect ship-based vertical profiles of temperature and salinity and the IORS-based time series of temperature, salinity, and pressure data observed at nominal depths of 2, 5, 11, 16, 22, 32, and 37 m, with a typical sampling time interval of 60 s (Ha et al., 2019). The data processing of CTD and UCTD were conducted same as SAVEX15 experiment. After removing outliers, the moored temperature and salinity data were vertically interpolated using the Akima spline method (Akima, 1970) with an interval of 1 m.

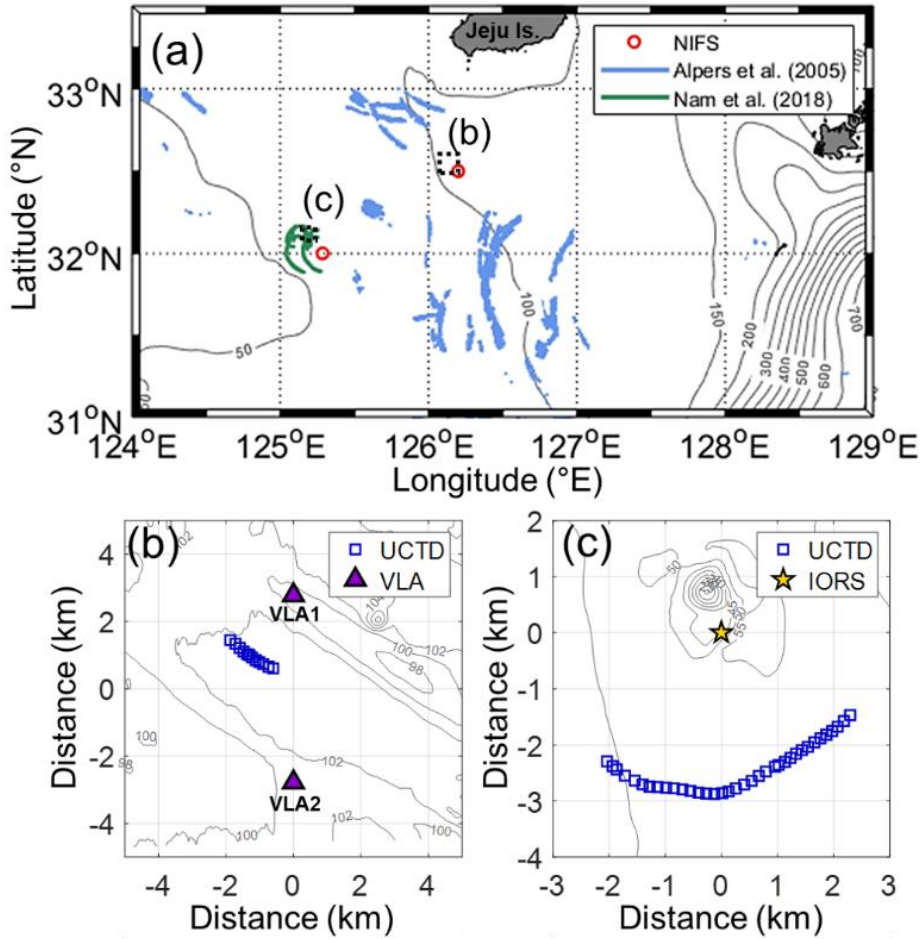


Figure 2.4. (a) Map showing the geographic region of this study for two areas of experiments (black dashed boxes), bathymetry (grey lines), and distribution of surface manifestation of NLIWs described by Alpers et al., 2006 (blue lines) and Nam et al., 2018 (green lines). Two stations conducting historical hydrographic data sampling for the National Institute of Fisheries Science (NIFS) used in this study are marked by red open circles. Zoomed-in maps of the two areas of (b) Shallow-water Acoustic Variability EXperiment 2015 (SAVEX15) and (c) Ieodo Ocean Research Station 2018 (IORS18). Locations of underway conductivity–temperature–depth (UCTD) data collection, moored observations (VLA1 and VLA2), and Ieodo Ocean Research Station (IORS) are marked by blue open squares in (b,c), purple triangles in (b), and yellow stars in (c).

Historically, vertical temperature and salinity profiles have been measured using the CTD, typically every other month at nominal hydrographic stations around the Korean peninsula, spanning a period of 60 years (Figure 2.5), and operated by the National Institute of Fisheries Science (NIFS), Republic of Korea. This study used the NIFS CTD data collected from 1990 to 2019 in the northern ECS (crosses in Figure 1.2). To ensure quality, excessive temperature and salinity data beyond global and local ranges were first removed. Then, the spike and gradient test's quality control procedures were applied to extract reliable salinity and temperature profiles only. Because the profiles are provided only at standard depths (surface, 10, 20, 30, 50, 75, 100, 125, 150, 200, and 250 m), linear interpolation was applied to obtain a vertical profile with an interval of 1 m.

The seasonal climatology temperature and salinity profiles from the World Ocean Atlas 2018 from the National Oceanographic Data Center, with a horizontal resolution of 0.25° grids at 102 standard vertical levels (0–5500 m), were used to calculate the density and stratification (Locarnini et al., 2018; Zweng et al., 2019). Because the temperature and salinity profile data are provided only at standard depths, similar linear interpolation was applied to obtain a vertical profile with an interval of 1 m.

Time-series data of sea level anomalies observed at the IORS ($32^\circ 7.4$ N, $125^\circ 10.9$ E, constructed at a water depth of 41 m; star in Figures 1.2 and 2.4) with a sampling interval of 10 min (Ha et al., 2019) were used. Barotropic semidiurnal tidal currents with a time interval of 1 h in the experimental area during this period were obtained using the Oregon State University Tidal Prediction Software with TPXO9-atlas (Egbert and Erofeeva, 2002). To visualize the effect of bottom topography on the generation and propagation of NLIWs, we used isobaths determined from the ETOPO1 database with a spatial resolution of 1 arc-min. The TPXO9 barotropic tidal currents, buoyancy frequency estimated using the climatology of water temperature and salinity data, and the ETOPO1 bathymetry data were linearly interpolated to estimate a depth-integrated, internal tide-generating body force at a horizontal resolution of 5 arc-min.

This study was used true-color images produced from calibrated, corrected, and geo-located radiance (Level-1 B) data from the Moderate-Resolution Imaging Spectroradiometer (MODIS) onboard the National Aeronautics and Space Administration satellites Terra and Aqua, with a spatial resolution of 250 m. The NLIWs induce divergence and convergence of sea surface currents as they propagate, which modifies the sea surface roughness and is thus visible in MODIS true-color

images if they are in a sun glint area (Jackson, 2007). The MODIS images were converted into grayscale, and a smooth front zone appeared as a bright band, whereas a rough front zone appeared as a dark band. Therefore, NLIWs are manifested as alternating bright and dark bands in the MODIS true-color images. This study used 93 images derived from the sea surface manifestations induced by NLIWs from 2015 to 2019. The propagation directions from the MODIS images were estimated from the horizontal curvature of the leading fronts from the sea surface manifestations. The propagation direction was calculated by the direction of the center of the straight line connecting the endpoints of the manifestations to the center of the arc of the manifestations (Lee and Nam, 2021; Wang et al., 2013). Among them, two images obtained by MODIS Terra on 2 August 2015, and MODIS Aqua on 30 July 2018, were used to estimate the propagation direction of NLIWs from sea surface manifestations to compare with estimation of propagation direction from observation data.

2.2. Two models and applications

2.2.1. Two-layered KdV (Korteweg-de Vries) models

For two-layered system, the environmental stratification parameters (ρ_1 , ρ_2 , h_1 , and h_2) for mode-1 NLIWs were estimated from the vertical structures of density and buoyancy frequency computed from the temperature and salinity using normal mode analysis (J. Klinck's MATLAB program `dynmodes.m`). The thicknesses of the upper and lower layers (h_1 and h_2) were determined from the first mode peak in vertical velocity (or zero-passing in the first mode horizontal velocity), and then the densities of the upper and lower layers (ρ_1 and ρ_2) were calculated by averaging the homogeneous densities within each layer. The maximum isotherm displacement or amplitude (η_0) of the NLIWs was determined from isotherms as a time period when the displacement of either isotherm exceeded 4 m in an hour.

In classical KdV theory (Korteweg and de Vries, 1895), a leading-order weak non-linearity and dispersion are competing but comparable to each other. For the two-layered KdV theory, the thicknesses (h_1 , h_2) and densities (ρ_1 , ρ_2) of the upper and lower layers can be used to estimate the parameters of mode-1 NLIWs, including linear phase speed $c_{KdV.l}$, theoretical propagation speed $c_{KdV.iw}$, characteristic width $2\Delta_{KdV.iw}$, nonlinear parameter α , and dispersion parameter β , yielding the wave equation as follows (Apel et al., 2007; Apel, 2003):

$$\frac{\partial \eta}{\partial t} + c_{KdV.l} \frac{\partial \eta}{\partial x} + \alpha \eta \frac{\partial \eta}{\partial x} + \beta \frac{\partial^3 \eta}{\partial x^3} = 0, \quad (2.1)$$

where η , t , and x are the vertical displacement of the isopycnals (or isotherms), time, and horizontal coordinates, respectively. The $c_{KdV.l}$, α , and β can be estimated using the density stratification parameters (ρ_1 , ρ_2 , h_1 , and h_2) in a two-layered system as follows:

$$c_{KdV.l} = \sqrt{g \frac{\rho_2 - \rho_1}{(\rho_1 + \rho_2)/2} \frac{h_1 h_2}{(h_1 + h_2)}} \quad (2.2)$$

$$\alpha = \frac{3}{2} \frac{c_{KdV.l} \rho_2 h_1^2 - \rho_1 h_2^2}{h_1 h_2 \rho_2 h_1 + \rho_1 h_2} \quad (2.3)$$

$$\beta = \frac{c_{KdV.l} h_1 h_2 \rho_1 h_1 + \rho_2 h_2}{6 \rho_2 h_1 + \rho_1 h_2} \quad (2.4)$$

Here, g is the gravity acceleration set to 9.80 m s^{-2} . The thicknesses of the upper and lower layers (h_1 and h_2) were determined based on the depth of the maximum density gradient from the density profiles obtained from the UCTD. The densities at the upper and lower layers (ρ_1 and ρ_2 , respectively) were determined as the minimum density within the upper layer and the maximum density within the lower layer, respectively. The solution of Equation (2.1) for the displacement $\eta(x, t)$ yields the nonlinear soliton as follows:

$$\eta(x, t) = \eta_0 \operatorname{sech}^2 \left(\frac{x - c_{KdV.iw} t}{\Delta_{KdV.iw}} \right). \quad (2.5)$$

Here, the theoretical propagation speed $c_{KdV.iw}$ and characteristic width $2\Delta_{KdV.iw}$ were calculated from the linear phase speed $c_{KdV.l}$ and the amplitude (η_0) of the vertical displacement of η are as follows:

$$c_{KdV.iw} = c_{KdV.l} + \frac{\alpha \eta_0}{3}, \quad (2.6)$$

$$2\Delta_{KdV.iw} = 2 \left(\frac{12\beta}{\alpha \eta_0} \right)^{1/2}. \quad (2.7)$$

By considering cubic nonlinearity, Equation (2.1) becomes as follows, yielding the extended KdV (eKdV) theory (Helfrich and Melville, 2006):

$$\frac{\partial \eta}{\partial t} + c_{KdV.l} \frac{\partial \eta}{\partial x} + \alpha \eta \frac{\partial \eta}{\partial x} + \alpha_1 \eta^2 \frac{\partial \eta}{\partial x} + \beta \frac{\partial^3 \eta}{\partial x^3} = 0. \quad (2.8)$$

Here, $\alpha_1 = \frac{3c_{KdV.l}}{(h_1 h_2)^2} \left[\frac{7}{8} \left(\frac{\rho_2 h_1^2 - \rho_1 h_2^2}{\rho_2 h_1 + \rho_1 h_2} \right)^2 - \left(\frac{\rho_2 h_1^3 + \rho_1 h_2^3}{\rho_2 h_1 + \rho_1 h_2} \right) \right]$ is a cubic nonlinear parameter in the two-layer system. The theoretical propagation speed $c_{eKdV.iw}$ and characteristic width $2\Delta_{eKdV.iw}$ based on the eKdV theory in the two-layered system are as follows:

$$c_{eKdV.iw} = c_{KdV.l} + \frac{\alpha\eta_0}{3} + \frac{\alpha_1\eta_0^2}{6}, \quad (2.9)$$

$$2\Delta_{eKdV.iw} = 2 \left(\frac{12\beta}{\alpha\eta_0 + 0.5\alpha_1\eta_0^2} \right)^{1/2}. \quad (2.10)$$

2.2.2. Empirical model

Jackson (2009) developed an empirical model and applied it to the NLIWs in the South China Sea, where the speed of NLIWs was parameterized as a function of water depth:

$$C(x, y) = A\sqrt{\tanh[B_1 + H(x, y)/B_2]} \quad (2.11)$$

where A is the wave speed parameter (m/s), $B_1 = 0.003$ and $B_2 = 1390.758$ m are empirical coefficients, and $H(x, y)$ is the local water depth specified by longitude x and latitude y . An envelope curve was applied to incorporate the nonlinear effects of the NLIWs to obtain $C(x, y)$ as a function of the water depth. The empirical model of Equation (2.11) was used to determine A by fitting the estimated propagation speed (detailed below) using Equation (2.6) from the vertical profiles of density (Figure 2.6).

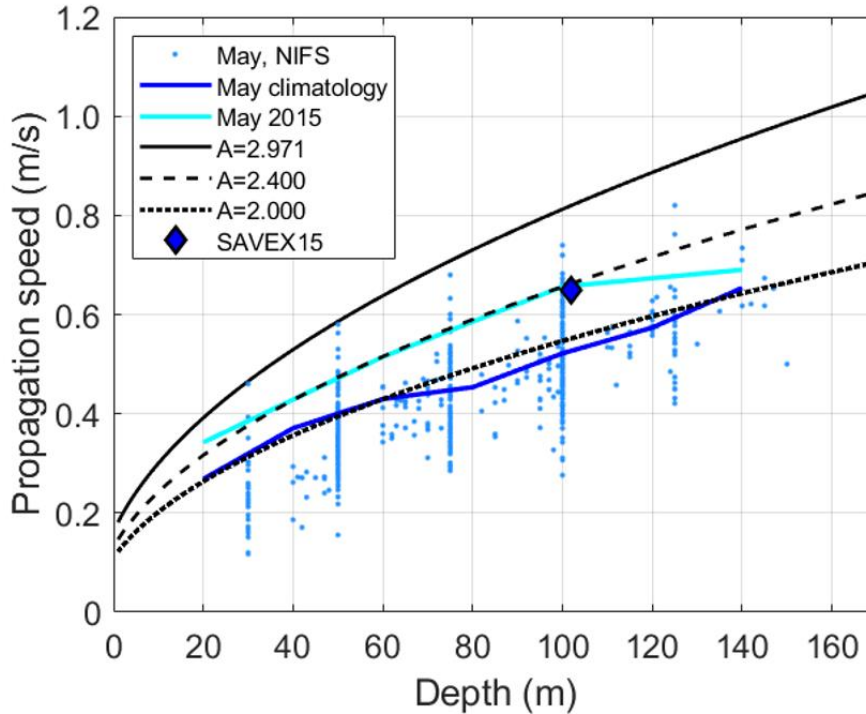


Figure 2.6. Propagation speed of nonlinear internal waves as function of water depth in northern East China Sea. The blue circles mean propagation speed of NLIW in May obtained from NIFS data, which is calculated two-layered KdV model at an amplitude of 6 m. The blue and cyan line mean the propagation speed of May climatology and May 2015, respectively. The solid black line means the empirical model from Jackson (2009), and dashed and dotted line mean modified A parameters of the empirical model to applicate in this study.

2.3 Estimation of propagation speed and direction

2.3.1. Estimation using moored and underway measurements

2.3.1.1. Doppler Shift method

To estimate the propagation direction of NLIWs using the Doppler shift caused by propagating NLIWs observed from a moving ship, the theoretical propagation speed $c_{KdV.iw}$ and ship speed v_{sh} were assumed to be constant during the measurement period, and the propagation direction was assumed to be orthogonal to the constant phase lines parallel to the wavefront lines (Figure 2.7a,b). As the estimated propagation direction ϕ_{ds} is in reference to the ship course ϕ_{sh} , the apparent propagation speed c_{ap} can be represented as the difference between $c_{KdV.iw}$ and the ship speed in direction θ_{ds} as follows:

$$c_{ap} = c_{KdV.iw} - v_{sh} \cos(\theta_{ds}). \quad (2.12)$$

Here, $\theta_{ds} = |\phi_{sh} - \phi_{ds}|$ is the angular difference between the ship course and the propagation direction of the NLIWs. Because the Doppler-shifted apparent frequency f_{ap} or the inverse of the apparent period T_{ap} can be represented by c_{ap} and $c_{iw} = \lambda_{KdV.iw} f_{iw}$, where $\lambda_{KdV.iw}$ is the wavelength of the NLIWs and the Doppler equation $f_{ap} = f_{iw} \frac{c_{ap}}{c_{iw}}$ (Kinsler et al., 1999), the following equation can be used to estimate the ϕ_{ds} :

$$\frac{1}{T_{ap}} = f_{ap} = f_{iw} \frac{c_{ap}}{c_{iw}} = \frac{c_{ap}}{\lambda_{KdV.iw}}. \quad (2.13)$$

Here, T_{ap} is determined from measurements, while $\lambda_{KdV.iw}$ is determined by the Cnoidal model (Apel, 2003) as

$$\lambda_{KdV.iw} = 2\Delta_{KdV.iw}K(s) \approx 3.7\Delta_{KdV.iw}, \quad (2.14)$$

where $K(s)$ is a complete elliptic integral of the first kind and parameter s is set to

0.5. Equation (2.12) can then be rewritten using Equation (2.13) as follows:

$$c_{KdV.iw} - v_{sh} \cos|\phi_{sh} - \phi_{ds}| = f_{ap}\lambda_{KdV.iw}. \quad (2.15)$$

Further, the ϕ_{ds} is obtained as follows:

$$\phi_{ds} = \phi_{sh} \pm \cos^{-1} \left(\frac{c_{KdV.iw} - f_{ap}\lambda_{KdV.iw}}{v_{sh}} \right). \quad (2.16)$$

The propagation direction of the NLIWs estimated using the method described above has an angular ambiguity caused by the sign of the arccosine part. Thus, a physically reasonable direction between the two was selected. The ϕ_{ds} and ϕ_{sh} are angles in degrees measured counter-clockwise from the east (for example, 180° and 270° correspond to the westward and southward directions, respectively).

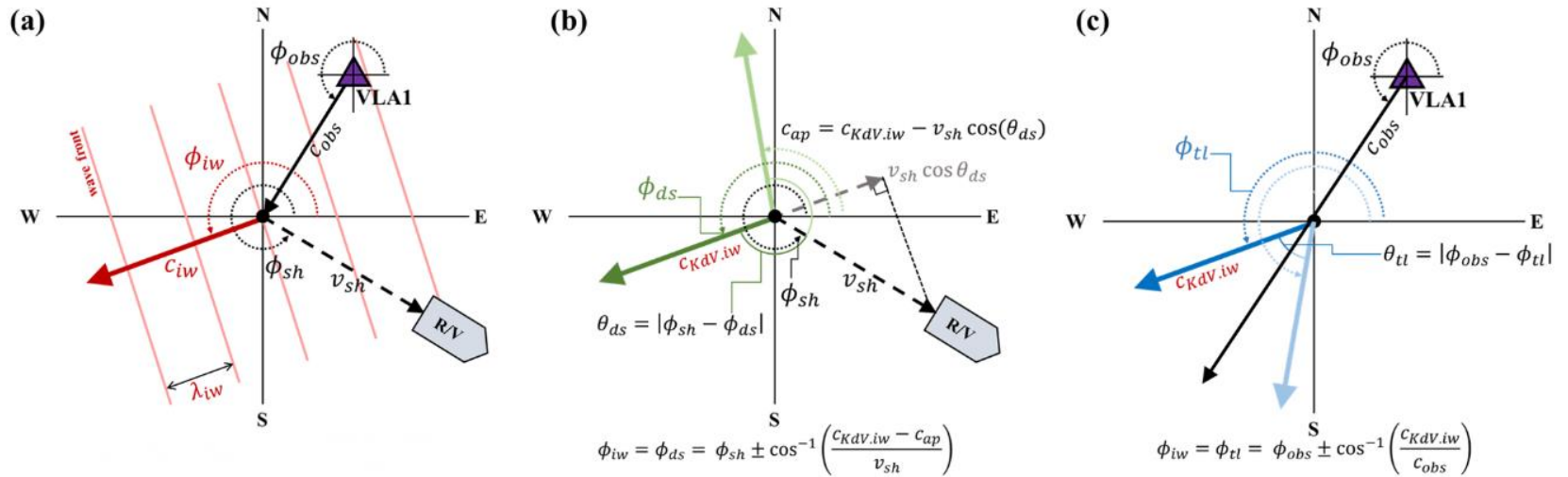


Figure 2.7. Schematic description of (a) the definition of parameters and estimation of the NLIW propagating direction based on the (b) Doppler shift and (c) time lag.

2.3.1.2. Time lag method

Independent of the method described in Section 2.3.1.1., the propagation direction of NLIWs was estimated using the distance between two locations of the NLIW front observed at different times, with the assumption that the NLIWs propagate across the two measurement locations with an angle orthogonal to the constant phase lines at a constant speed (Figure 2.7a,c). The observed propagation speed was estimated by dividing the distance between the two locations D_{obs} by the arrival time lag T_{obs} , for example, $c_{obs} = \frac{D_{obs}}{T_{obs}}$. Then, $c_{KdV.iw}$ was calculated from c_{obs} and angular difference $\theta_{tl} = |\phi_{obs} - \phi_{tl}|$ between ϕ_{obs} (direction from the first measurement location to the second measurement location) and the propagation direction of NLIWs ϕ_{tl} as

$$c_{KdV.iw} = c_{obs} \cos(\theta_{tl}) = \frac{D_{obs}}{T_{obs}} \cos(|\phi_{obs} - \phi_{tl}|). \quad (2.17)$$

Finally, the ϕ_{tl} was obtained from Equation (2.17) as

$$\phi_{tl} = \phi_{obs} \pm \cos^{-1}\left(\frac{c_{KdV.iw}T_{obs}}{D_{obs}}\right). \quad (2.18)$$

The propagation direction estimated using the method described above (time lag method) also has an angular ambiguity caused by the sign of the arccosine part. Thus, a physically reasonable direction is selected. The ϕ_{tl} and ϕ_{obs} are angles in degrees measured counter-clockwise from the east.

2.3.1.3. Optimal propagation direction and successive propagation speed

Two propagation directions of NLIWs estimated from the two methods were used to estimate the optimal propagation direction and successive propagation speed. First, a consistent direction between the two directions derived from each method was selected to minimize the ambiguity where the two methods yield angular difference $|\phi_{ds} - \phi_{tl}|$ typically less than 30° . For example, each one (bold green and blue colors in Figure 2.7b,c) among two ϕ_{ds} and two ϕ_{tl} are selected as more consistent between the two methods and physically reasonable, while inconsistent ϕ_{ds} and ϕ_{tl} (deemed green and blue colors in Figure 2.7b,c) among the two ϕ_{ds} and two ϕ_{tl} were not selected. To optimize the propagation speed and direction, the difference in consistent propagation directions from the two methods $|\phi_{ds} - \phi_{tl}|$ was minimized by iteratively changing $c_{KdV.iw}$ at intervals of 0.01 m s^{-1} instead of using the constant propagation speed derived from the two-layered KdV theory. The updated propagation speed was determined from the iterations, and the final propagation direction of NLIWs ϕ_{iw} was determined by averaging the two directions $(\phi_{ds} + \phi_{tl})/2$ when $|\phi_{ds} - \phi_{tl}|$ reached its minimum value for the updated propagation speed. Iterations were performed for a range of 30% deviation from $c_{KdV.iw}$ (typically requiring 38 iterations to reach the minimum), which is comparable to the range of the interannual variation of propagation speed reported in a previous study (Cho et al., 2016).

2.3.1.4. Estimation of propagation direction using satellite

The propagation directions from the MODIS images (Figure 2.8) were estimated from the horizontal curvature of the leading fronts from the sea surface manifestations (Wang et al., 2013). The propagation direction was calculated by the direction of the center of the straight line connecting the endpoints of the manifestations to the center of the arc for the manifestations. For example, a manifestation of NLIW is shown in the blue box in Figure 2.8a,c. The orange curvature line from both endpoints (Points A and B) is the leading front of the NLIW. Point C is the center of line AB. Point D is the center of the arc AB. In this case, the angle between the vectors from C to D, measured counter-clockwise from the east, is the propagation direction.

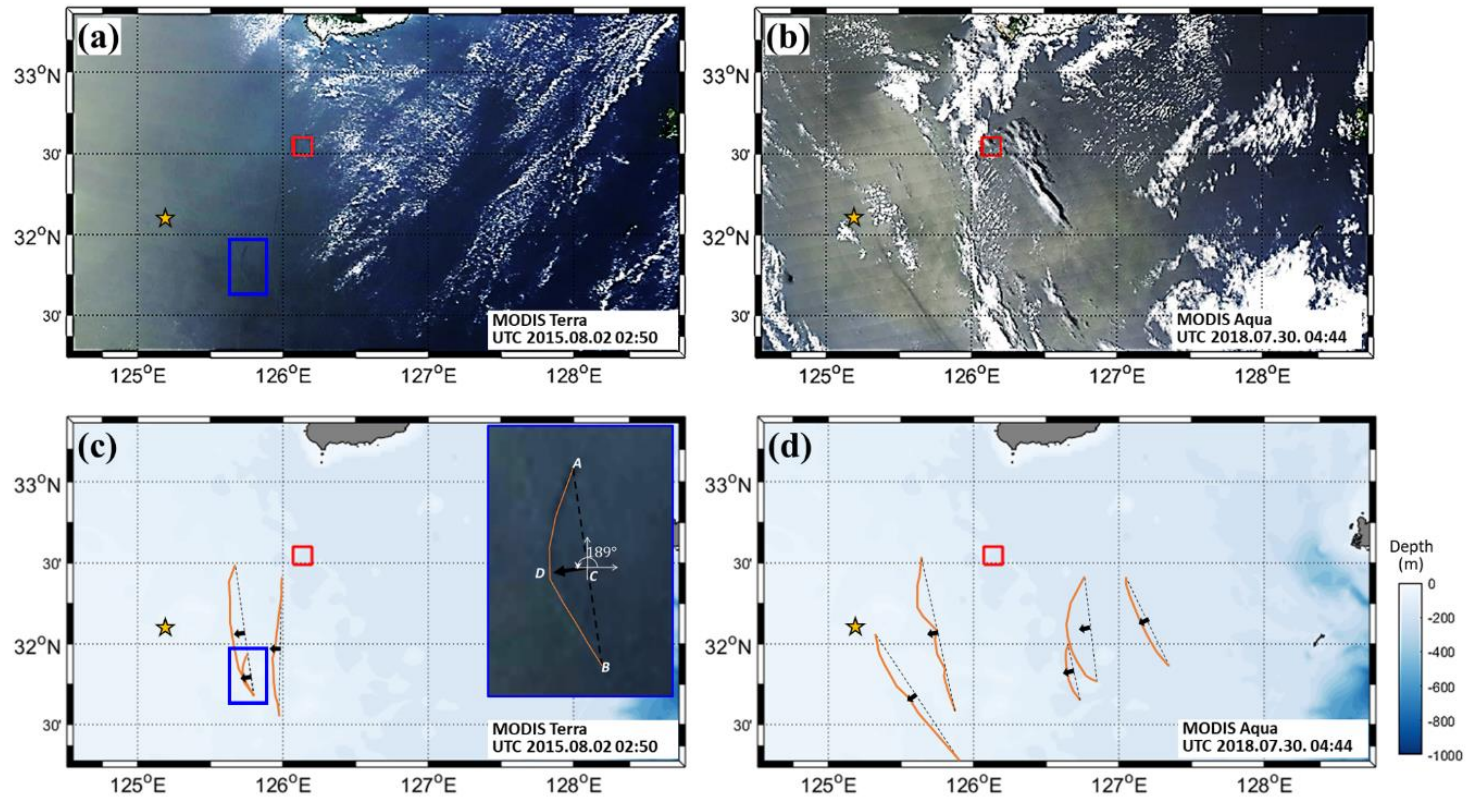


Figure 2.8. (a,b) Two satellite images where (c,d) surface manifestations of NLIWs (orange lines) are confirmed, from MODIS Terra at 02:50 UTC on 02 August 2015, and MODIS Aqua at 04:44 UTC on 30 July 2018. The blue box is the example of the propagation direction calculation. The SAVEX15 and IORS are marked by a red box and yellow star, respectively.

2.3.2. Applications

2.3.2.1. SAVEX15

On 23 May 2015 during the SAVEX15, the existence of NLIWs was confirmed from a series of UCTD profiling measurements, for example, at 15:56 UTC (vertical red dashed line in Figure 2.9b), and the time-depth pattern of temperature variations observed at the northern mooring VLA1 at 15:02 UTC (vertical grey dashed line in Figure 2.9a). The NLIW was observed at VLA1 3239 s earlier than that observed in the UCTD measurements (Figures 2.9 and 2.10a). The 13 °C isotherm displacements, derived from the UCTD and VLA1 observations, commonly range from 27 to 35 m (Figure 2.10a). The NLIW has an amplitude (η_0) of 6.1 and 5.9 m estimated from UCTD and VLA1 observations, respectively (Figures 2.9 and 2.10a). The two-layered theoretical parameters of the NLIWs are listed in Table 2.1, along with the estimated parameters, where the upper and lower layer densities (ρ_1 and ρ_2) are 1023.35 and 1025.17 kg m⁻³, respectively, and the upper and lower layer thicknesses (h_1 and h_2) are 34.8 and 65.2 m, respectively (Figure 2.10b and Table 2.1).

When the ship moved at a speed of 0.47 m s⁻¹ and a direction of 148° (northwestward), the apparent propagation direction ϕ_{ds} of NLIWs had an angular difference θ_{ds} of $\pm 60^\circ$ with ship course ϕ_{sh} (Figure 2.11a), derived from the Doppler shift method using Equation (2.16), resulting in $\phi_{ds} = 208^\circ$ (southwestward) or $\phi_{ds} = 88^\circ$ (northward). From the distance ($D_{obs} = 2233$ m) between the two measurement locations (VLA1 and ship) and the time lag of the NLIW arrivals ($T_{obs} = 3239$ s), the observed propagation direction of NLIWs ϕ_{tl} was estimated to have an angular difference θ_{tl} of $\pm 19^\circ$ with ϕ_{obs} (Figure 2.11b),

derived from the time lag method using Equation (2.18), resulting in $\phi_{tl} = 211^\circ$ (southwestward) or $\phi_{tl} = 249^\circ$ (slightly more southwestward). Thus, more consistent propagation directions of $\phi_{ds} = 208^\circ$ and $\phi_{tl} = 211^\circ$ were selected to optimize the propagation speed and direction. By minimizing $|\phi_{tl} - \phi_{ds}|$, the optimal propagation speed (c_{iw}) of 0.64 m s^{-1} was derived from the iterative calculations, yielding $\phi_{ds} = 208^\circ$ and $\phi_{tl} = 211^\circ$ with $|\phi_{tl} - \phi_{ds}| = 3^\circ$, and the resultant propagation direction (ϕ_{iw}) of 210° (southwestward).

Table 2.1. Nonlinear internal wave parameters for the two cases observed, with calculated and estimated values.

Parameters		SAVEX15	IORS18
Observation			
ρ_1 (kg · m ⁻³)	Upper layer density	1023.35	1018.18
ρ_2 (kg · m ⁻³)	Lower layer density	1025.17	1024.99
h_1 (m)	Upper layer thickness	34.8	24.0
h_2 (m)	Lower layer thickness	65.2	28.0
η_0 (m)	Wave amplitude	-6.1	-7.0
T_{ap} (sec)	Wave apparent period	1695	237
ϕ_{sh} (°)	Ship course	148	334
v_{sh} (m · s ⁻¹)	Ship speed	0.47	1.38
T_{obs} (sec)	Time lag between two different observations	3239	2370
D_{obs} (m)	Distance between two different observations	2233	3045
C_{obs} (m · s ⁻¹)	Speed between two different observations	0.69	1.29
ϕ_{obs} (°)	Angle between two different observations	230	243
Estimation base on KdV and eKdV theory			
α (s ⁻¹)	Nonlinear parameter	-0.0127	-0.0041
α_1 (s ⁻¹ · m ⁻¹)	Cubic nonlinear parameter	-0.0009	-0.0011
β (m ³ · s ⁻¹)	Dispersion parameter	238	104
$c_{KdV.l}$ (m · s ⁻¹)	Linear phase speed	0.63	0.92
$c_{KdV.iw}$ (m · s ⁻¹)	Propagating speed based on KdV theory	0.65	0.93
$c_{eKdV.iw}$ (m · s ⁻¹)	Propagating speed based on eKdV theory	0.65	0.92
$\Delta_{KdV.iw}$ (m)	Characteristic width based on KdV theory	384	416
$\Delta_{eKdV.iw}$ (m)	Characteristic width based on eKdV theory	432	1182
$\lambda_{KdV.iw}$ (m)	Wavelength based on KdV theory	712	772
$\lambda_{eKdV.iw}$ (m)	Wavelength based on eKdV theory	802	2192
Estimation based on proposed methods (KdV theory)			
θ_{ds} (°)	Angle between ϕ_{ds} and ϕ_{sh}	60	126
ϕ_{ds} (°)	NLIW propagating direction from Doppler shift	208	208
θ_{tl} (°)	Angle between ϕ_{tl} and ϕ_{obs}	19	45
ϕ_{tl} (°)	NLIW propagating direction from time lag	211	198
c_{iw} (°)	Optimal NLIW propagating speed	0.64	1.06
ϕ_{iw} (°)	Optimal NLIW propagating direction	210	205
Estimation based on proposed methods (eKdV theory)			
θ_{ds} (°)	Angle between ϕ_{ds} and ϕ_{sh}	68	100
ϕ_{ds} (°)	NLIW propagating direction from Doppler shift	215	235
θ_{tl} (°)	Angle between ϕ_{tl} and ϕ_{obs}	18	46
ϕ_{tl} (°)	NLIW propagating direction from time lag	212	197
c_{iw} (°)	Optimal NLIW propagating speed	0.66	1.30
ϕ_{iw} (°)	Optimal NLIW propagating direction	213	234

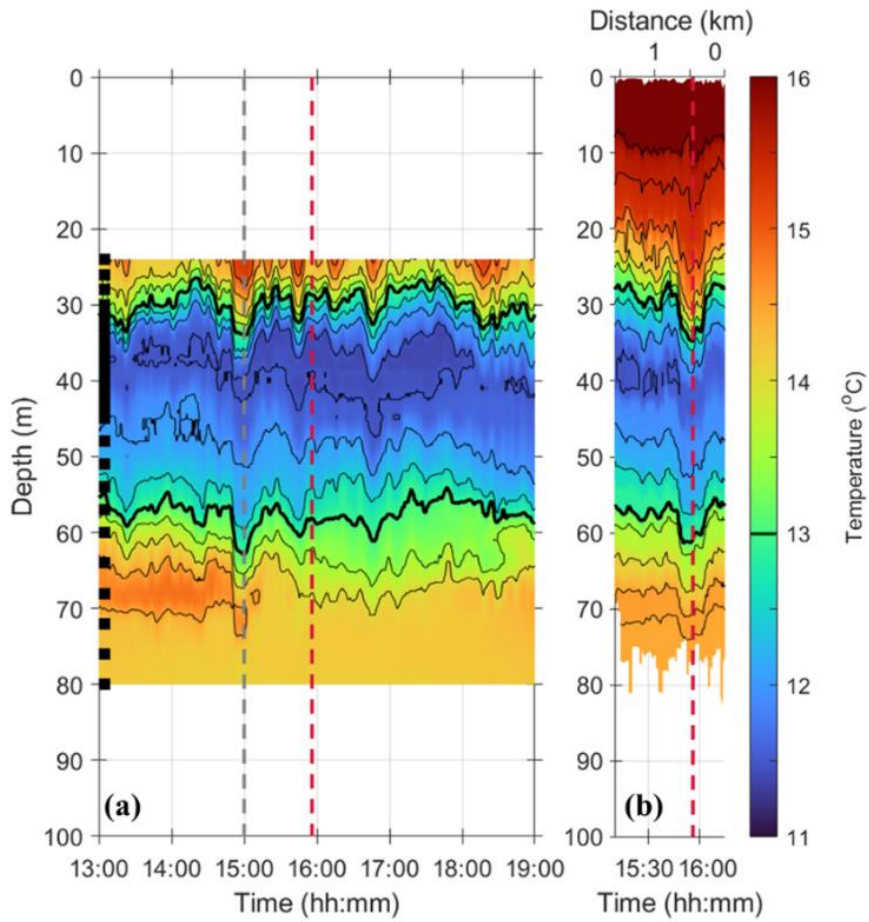


Figure 2.9. Time-depth pattern of water temperature observed from (a) northern mooring (VLA1) and (b) UCTD during the SAVEX15. The contour interval is 0.5 °C. The 13 °C isotherm is denoted by a thick black line. The times of NLIW observations at the VLA1 and UCTD are denoted by vertical grey and red dashed lines, respectively. Depths of thermistors attached to the VLA1 are denoted by black squares on the left axes.

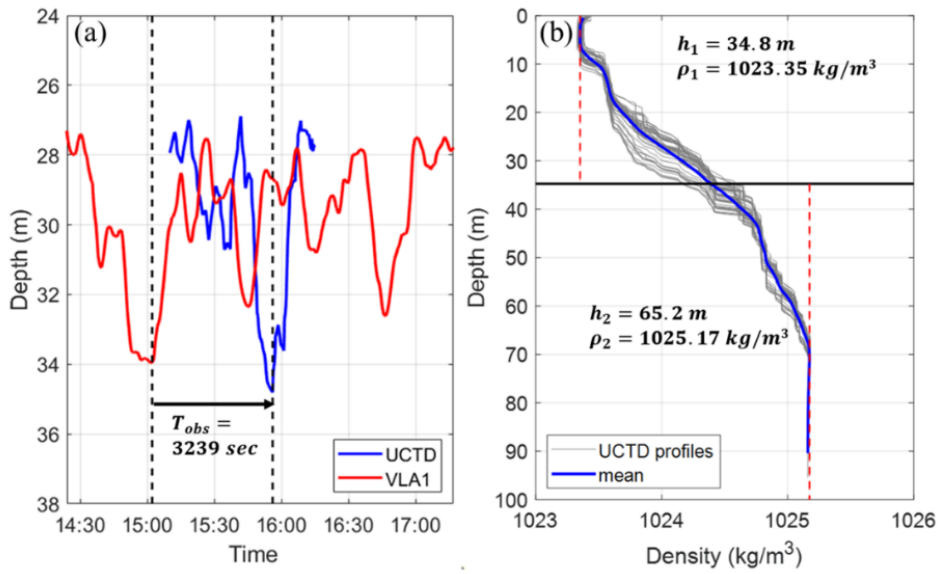


Figure 2.10. (a) Time-series of 13 °C isotherm depth observed at the VLA1 (red) and UCTD (blue), and (b) vertical profiles of density obtained from the UCTD measurements (grey) at 15:10–16:14 UTC on 23 May 2015. In (b), the average profile is marked in blue, and minimum and maximum densities at the upper and lower layers (corresponding to ρ_1 and ρ_2), respectively, are shown with red dashed lines.

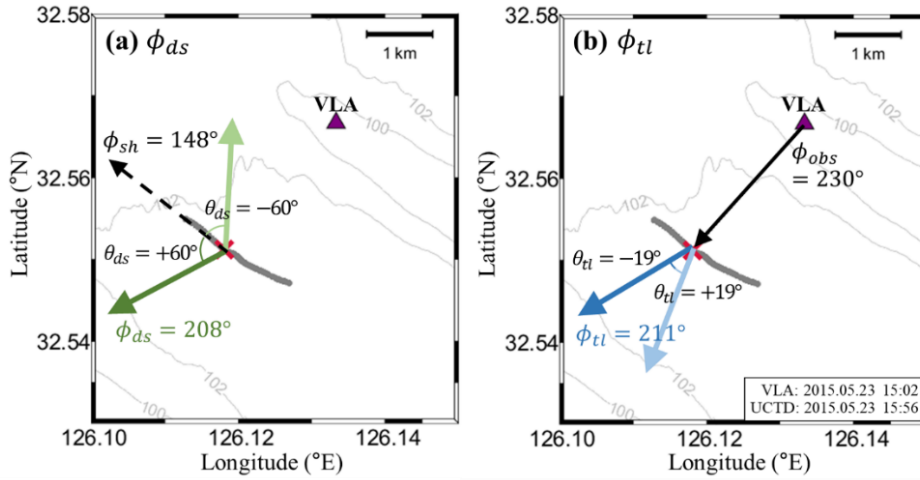


Figure 2.11. Propagation direction of NLIW observed during the SAVEX15, estimated from (a) Doppler shift method and (b) time lag method. The ϕ_{sh} , ϕ_{obs} , θ_{ds} , and θ_{tl} are labelled in the plots. Date and times of the corresponding events are noted in the right bottom corner.

2.3.2.2. IORS18

On 30 August 2018 during the IORS18, the existence of NLIWs was confirmed from the isotherm displacements observed by a series of vertical profiling UCTD measurements, particularly at 11:11 UTC (vertical red dashed line in Figure 2.12b), and the time-depth pattern of temperature measurements at the IORS, at 10:32 UTC (vertical grey dashed line in Figure 2.12a). The NLIWs observed at IORS were 2370 s earlier than those observed at the UCTD (Figure 2.13a). The 18 °C isotherm displacements observed from the UCTD and IORS were comparable, ranging from 23 to 31 m (Figure 2.13a). The NLIWs (the leading NLIW among a set observed by the UCTD) had an amplitude (η_0) of 6.8 and 7.0 m derived from the IORS and UCTD observations, respectively (Figures 2.12 and 2.13a). The densities at the upper and lower layers (ρ_1 and ρ_2) were 1018.18 and 1024.99 kg m⁻³, and thicknesses of the upper and lower layers (h_1 and h_2) were 24.0 and 28.0 m, respectively (Figure 2.13b and Table 2.1).

When the ship moved at a speed of 1.38 m s⁻¹ and a direction of 334° (southeastward), the apparent propagation direction ϕ_{ds} of NLIWs had the angular difference θ_{ds} of $\pm 126^\circ$ with the ship course ϕ_{sh} (Figure 2.14a), derived from the Doppler shift method using Equation (2.16), resulting in $\phi_{ds} = 208^\circ$ (southwestward) or $\phi_{ds} = 100^\circ$ (northward). From the distance ($D_{obs} = 3045$ m) between the two measurement locations (IORS and ship) and the time lag of the NLIW arrivals ($T_{obs} = 2370$ s), the observed propagation direction of NLIW ϕ_{tl} was estimated to have an angular difference $\theta_{tl} = \pm 45^\circ$ with ϕ_{obs} (Figure 2.14b), derived from the time lag method using Equation (2.18), resulting in $\phi_{tl} = 198^\circ$ (southwestward) or $\phi_{tl} = 288^\circ$ (southeastward). Thus, more consistent propagation

directions of $\phi_{ds} = 208^\circ$ and $\phi_{tl} = 198^\circ$ were selected to optimize the propagation speed and direction. By minimizing $|\phi_{tl} - \phi_{ds}|$, optimal propagation speed (c_{iw}) of 1.06 m s^{-1} was derived from the iterative calculations, yielding $\phi_{ds} = 205^\circ$ and $\phi_{tl} = 205^\circ$ with $|\phi_{tl} - \phi_{ds}| = 0^\circ$, and the resulting propagation direction (ϕ_{iw}) of 205° was obtained.

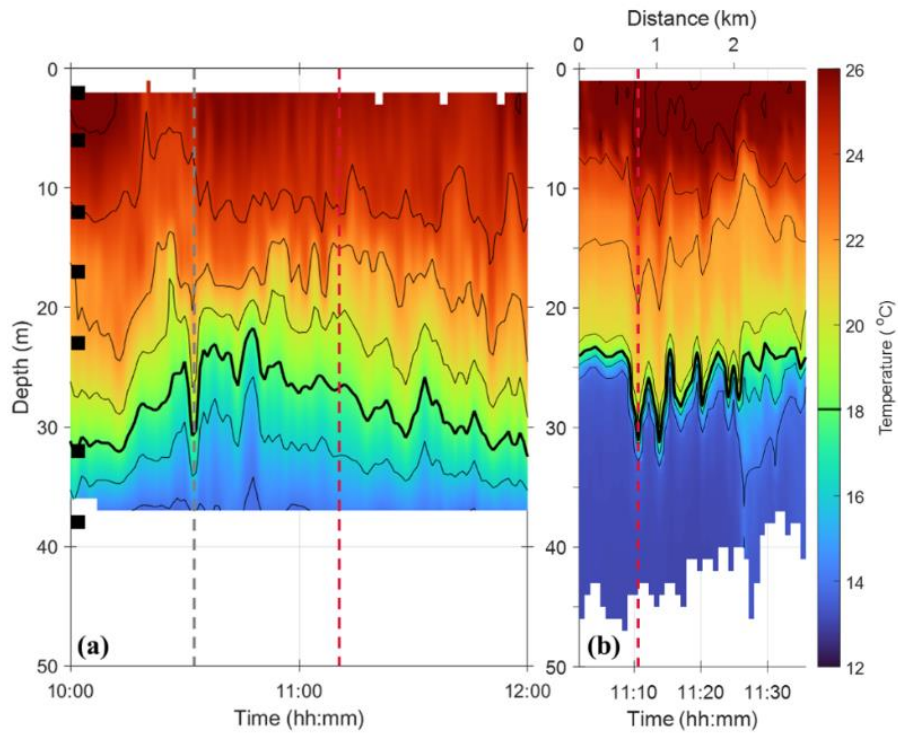


Figure 2.12. Time-depth pattern of water temperature observed at the (a) IORS and (b) UCTD during IORS18. The contour interval is 2 °C. The 18 °C isotherm is denoted by a thick black line. Time of NLIW observations at the IORS and UCTD are denoted by vertical grey and red dashed lines, respectively. Depths of thermistors attached to the IORS are denoted by black squares on the left axes.

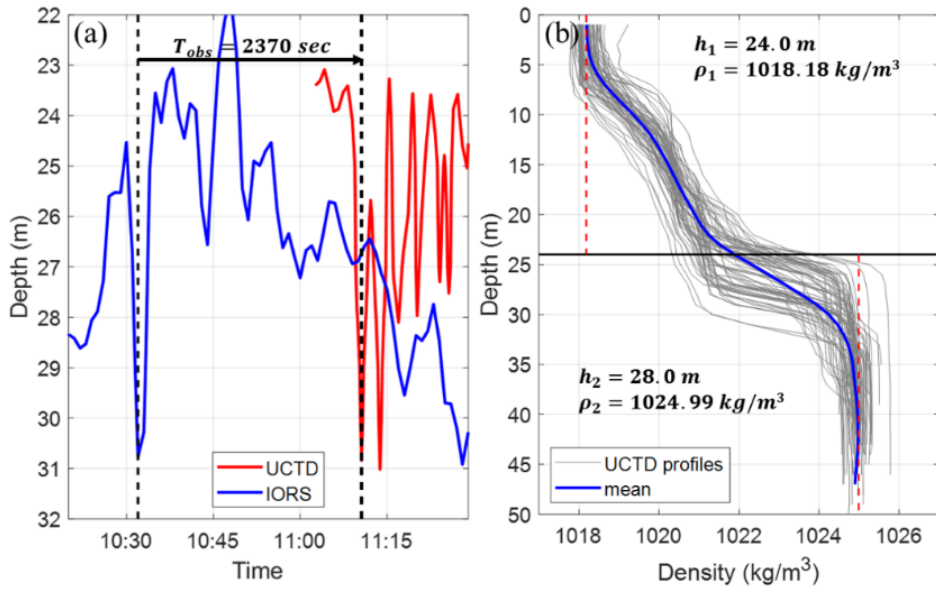


Figure 2.13. Information related to NLIWs observed at the IORS and UCTD during IORS18. (a) Time-series of the depth of the 18 °C isotherm observed at the IORS (red) and UCTD (blue), and (b) vertical profiles of density obtained from the UCTD measurements (grey) at 11:02–11:59 UTC on 30 August 2018. In (b), the average profile is marked in blue, and minimum and maximum densities at the upper and lower layers (corresponding to ρ_1 and ρ_2), respectively, are shown with red dashed lines.

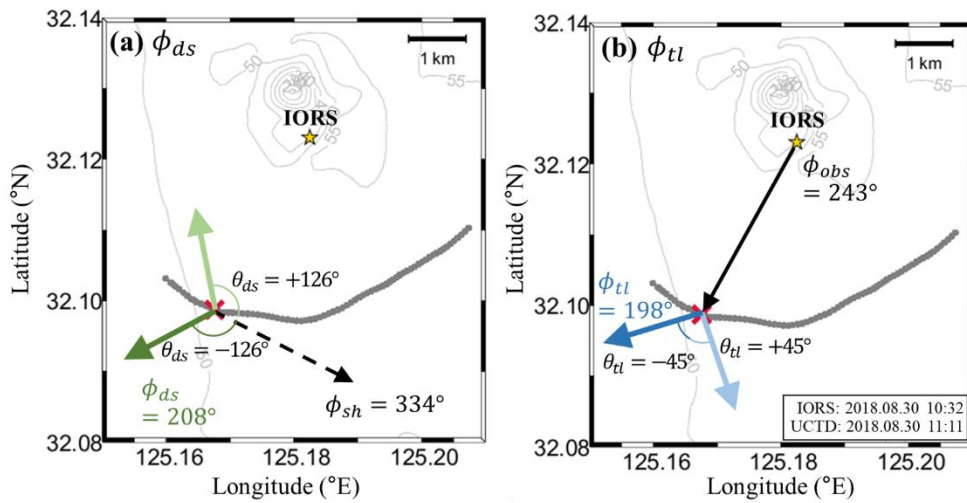


Figure 2.14. Propagation direction of NLIW observed during IORS18, estimated from (a) Doppler shift method and (b) time lag method. The ϕ_{sh} , ϕ_{obs} , θ_{ds} , and θ_{tl} are labeled in the plots. Dates and times of the corresponding events are noted in the right bottom corner.

2.3.3. Assessment

2.3.3.1. Propagation speed

Herein, I discussed whether the propagation speeds of NLIWs estimated using the proposed method are reasonable based on the KdV theory and previous observations. Interannual variations of the theoretical propagation speed ($c_{KdV.iw}$, NIFS-SAVEX15) in May from 1994 to 2019 derived from the NIFS historical hydrographic data near the SAVEX15 area range from 0.36 to 0.71 m s^{-1} , with a temporal mean and standard deviation of 0.50 and 0.09 m s^{-1} , respectively (red line in Figure 2.15a). A long-term decreasing trend was observed in May $c_{KdV.iw}$ (NIFS-SAVEX15) at a rate of $-0.004 \text{ m s}^{-1} \text{ yr}^{-1}$ (red dotted line in Figure 2.15a), primarily because of the decreasing density stratification, that is, increasing ρ_1 and decreasing ρ_2 with no significant change in h_1 and h_2 in May (red lines in Figure 2.15b,c). The propagation speed for May 2015 estimated using the proposed method (c_{iw}) was consistent with the theoretical propagation speed ($c_{KdV.iw}$; SAVEX15) derived from the hydrographic data obtained during SAVEX15 and that (NIFS-SAVEX15) derived from the nearby NIFS data, with minor ($<0.05 \text{ m s}^{-1}$) differences (closed square, open square, and open circle in Figure 2.14a).

Similarly, interannual variations in the theoretical propagation speed ($c_{KdV.iw}$, NIFS-IORS18) in August from 1994 to 2019 derived from the NIFS historical hydrographic data near the IORS ranged from 0.42 to 0.86 m s^{-1} , with a temporal mean and standard deviation of 0.66 and 0.10 m s^{-1} , respectively (blue line in Figure 2.15a). However, the long-term trend in August $c_{KdV.iw}$ (NIFS-IORS18) was positive (at a rate of $0.003 \text{ m s}^{-1} \text{ yr}^{-1}$; blue dotted line in Figure 2.15a) because of the increasing density stratification between the layers, that is, decreasing ρ_1 and

increasing ρ_2 with no significant change in h_1 and h_2 in August (blue lines in Figure 2.15b,c). In contrast to May 2015, the propagation speed for August 2018 estimated using the proposed method (c_{iw}) was not consistent with the theoretical propagation speed ($c_{KdV.iw}$; IORS18) derived from the hydrographic data obtained during IORS18 and that (NIFS-IORS18) derived from the nearby NIFS data, yielding significant ($>0.25 \text{ m s}^{-1}$) differences (closed square, open square, and open circle in Figure 2.15a). The difference in density stratification between the NIFS and IORS18 data cannot explain the difference in c_{iw} from the theoretical propagation speeds of $c_{KdV.iw}$ (IORS18) and $c_{KdV.iw}$ (NIFS-IORS18), implying the limitation of theoretical estimation. A similar difference in the observed propagation speed from the theoretical propagation speed in the area near the IORS was reported from the observations in August 2005 (blue diamond in Figure 2.15) (Lee et al., 2006).

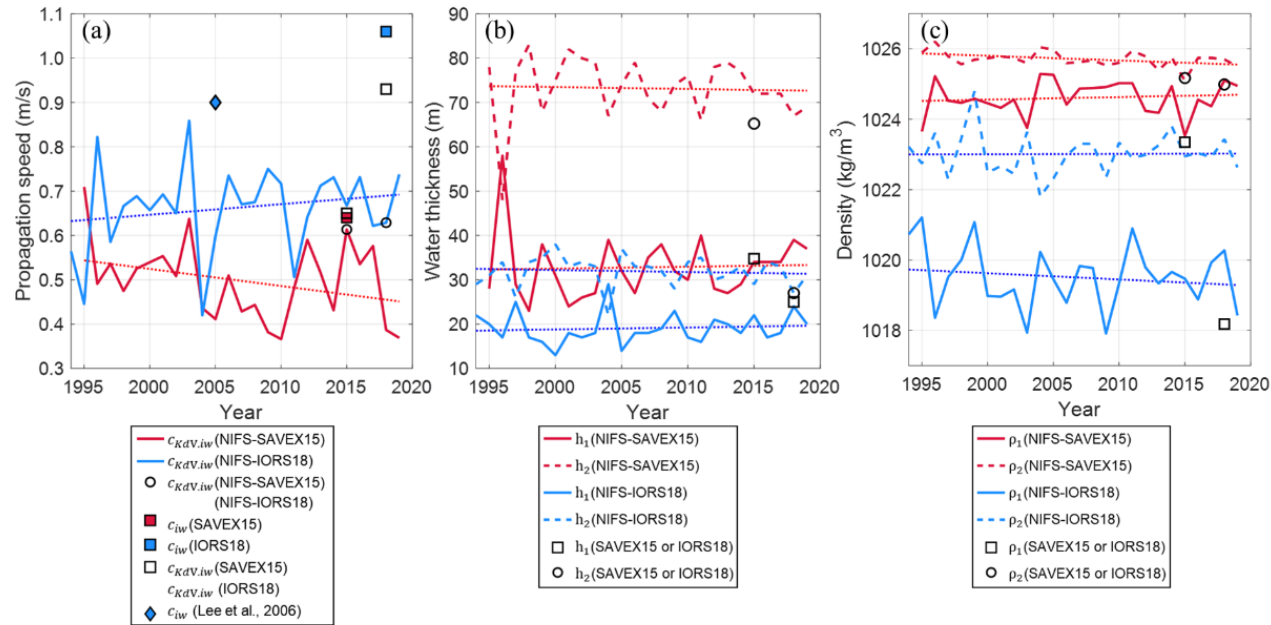


Figure 2.15. (a) Time series of propagation speed estimated from the method proposed in this study (colored squares; red for SAVEX15 and blue for IORS18) and KdV theory (open squares, open circles, and colored lines). KdV theory was applied using the NIFS historical hydrographic data for May (red line and open circle) and August (blue line and open circle), and hydrographic data obtained during SAVEX15 and IORS18 (open squares). The propagation speed of NLIWs observed in the northern ECS in August 2005 (Lee et al., 2006) is denoted by a blue diamond. Time series of (b) thickness (h_1 and h_2) and (c) density (ρ_1 and ρ_2) of the upper (solid lines) and lower (dashed lines) layers derived from the NIFS historical hydrographic data for May (red) and August (blue), and hydrographic data obtained during SAVEX15 and IORS18 (open squares and circles for upper and lower layers, respectively). Long-term trends of (a) propagation speed, (b) layer thickness, and (c) layer density from 1994 to 2019 are remarked with dotted lines.

2.3.3.2. Propagation direction

To determine whether the propagation directions of NLIWs estimated using the proposed method are physically reasonable, I compared the ϕ_{iw} values with those derived from satellite images and previous observations. The ϕ_{iw} values estimated during the two experiments (SAVEX15 and IORS18) using the proposed method were consistent with those derived from MODIS images. Despite the fact that the surface manifestations of NLIWs observed in the two MODIS images were distant (56–123 km from the SAVEX15 area and 42–190 km from the IORS) from the locations of NLIWs observed during the two experiments, south-westward-propagating NLIWs (propagation direction of 186–209°) were consistently found in the two images (Figure 2.8). Previous observations based on satellite SAR and optical images taken between 1993 and 2004 (Alpers et al., 2005) and SAR images taken between 2014 and 2015 (Nam et al., 2018) in the northern ECS also support the south-westward-propagating NLIWs (propagation direction ranging from 212° to 245°), which may be dominant among the various NLIWs propagating in multiple directions from multiple sources in the northern ECS. Although this proposed method gives reasonable results of propagation speed and direction, the two-layered KdV theory used in this study has clear limitations (discussed detail in Section 3.4). Also, an assumption of plain internal wave front (Figure 2.7a) in doppler method and time lag method is not fully realistic, although reasonable in two cases, because the NLIWs of various form (e.g., arc-like or parabolic forms originating from a single point or a line) have been examined using from satellite observations.

3. Results and discussions

3.1. Characteristics of NLIW in the northern ECS

3.1.1. Observed NLIWs

The NLIWs observed during the SAVEX15 using two VLAs (Figure 3.1), and UCTD data (Figure 3.2) were characterized by their amplitudes, periods, direction and speed of propagation, and characteristic width. Three events of NLIWs (E1, E2, and E3) observed from the UCTD matched the corresponding events of NLIWs observed at VLA1 and VLA2 (Figure 3.3). The NLIWs observed at UCTD and VLA1 during the E1 (Figures 3.2a and 3.3a) with $\eta_0 = -4.2$ m and $T_{app} = 575$ sec were addressed to propagate southwestward ($\phi_{ds} = 209^\circ$, $\phi_{tl} = 233^\circ$, and optimal direction of 212°) with the optimal propagation speed of 0.57 m s⁻¹ (Figure 3.4a and Table 3.1). Those observed during the E2 (Figures 3.2b and 3.3b) and E3 (Figures 3.2c and 3.3c) have similar characteristics, yielding ranges of propagating speed of 0.57 – 0.73 m s⁻¹ and propagating directions of 210 – 222° (southwestward), amplitude of 4.2 – 6.1 m, characteristic width of 384 – 592 m, and a southwest propagating direction that was consistent (210 – 222°) between the events (Table 3.1).

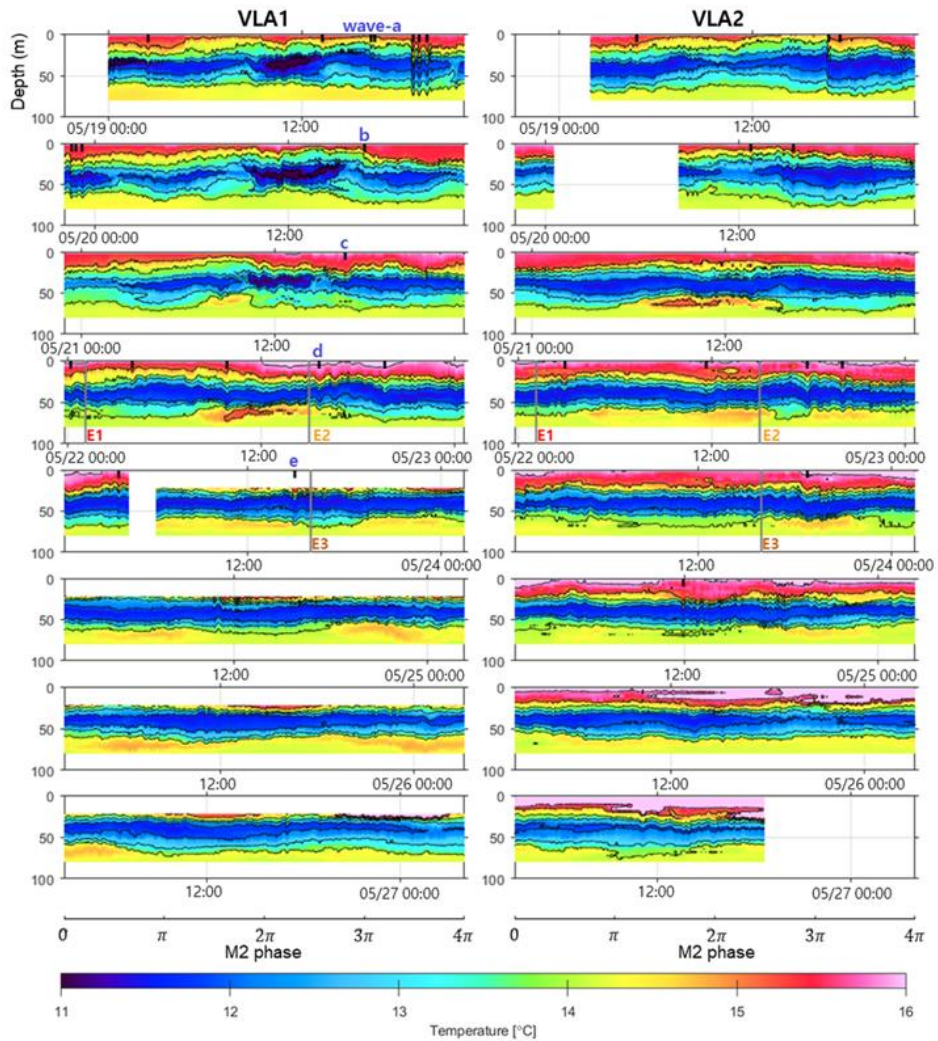


Figure 3.1. Time–depth contours of water temperature observed from VLA1 (left) and VLA2 (right) during SAVEX15. The time is separated by double M2 tidal periods (2 times 12.42 h) as indicated by the x-axes at the bottom. Timings of the NLIWs observed from the VLAs and UCTD are shown with thick black tick markers on the top x-axis and green vertical lines (labeled E1, E2, and E3), respectively.

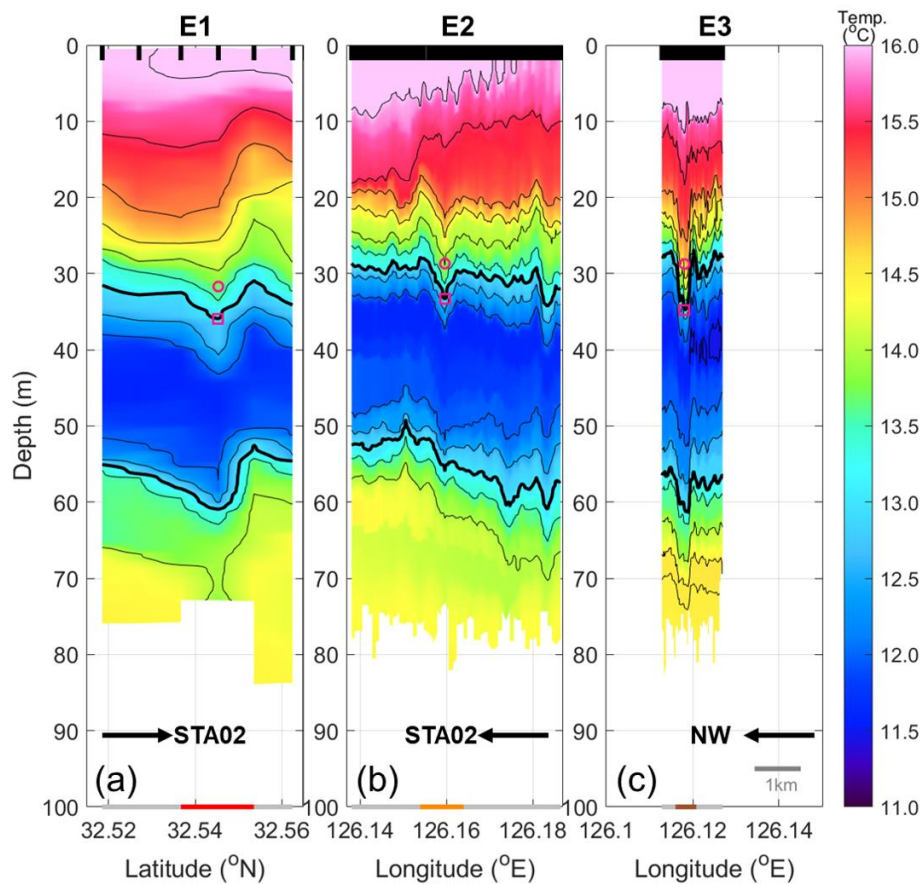


Figure 3.2. Cross-sectional structures of water temperature observed from UCTD during (a) E1, (b) E2, and (c) E3. The contour interval is 0.5 $^{\circ}$ C and the 13 $^{\circ}$ C isotherms are denoted by thick black lines. Maximum and minimum isotherm depths displaced by the NLIWs are indicated with red squares and circles, respectively. Timings of the UCTD profiling are noted with thick black tick markers on the top x-axis. The NLIW events and directions of ship movement during the UCTD profiling are marked with colored lines on the bottom x-axis and black horizontal arrows, respectively. The scale bar for 1 km is shown in the bottom right corner.

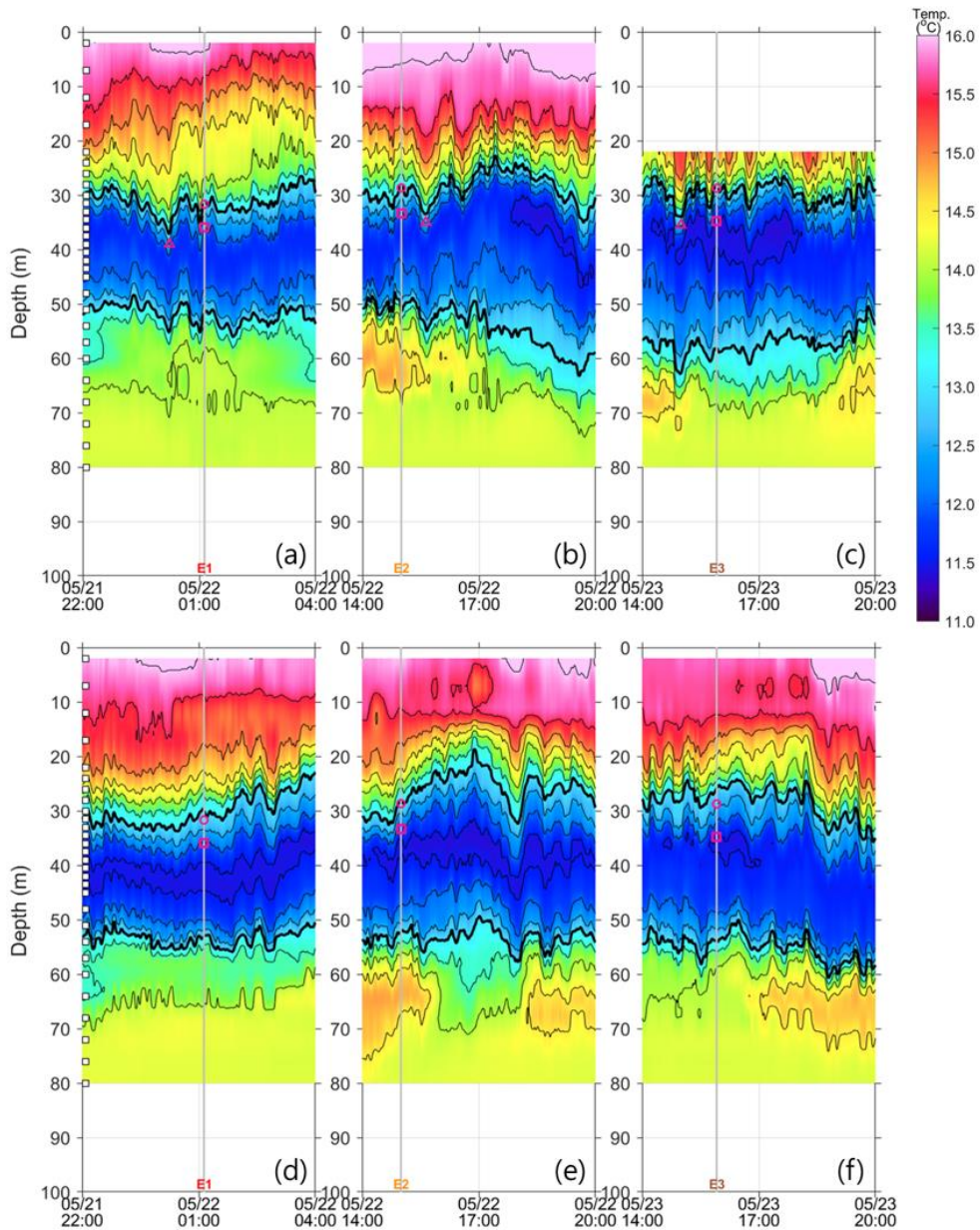


Figure 3.3. Time–depth contours of water temperature observed from (top) VLA1 and (bottom) VLA2 during the NLIWs events of (a, d) E1, (b, e) E2, and (c, f) E3. The contour interval is 0.5 °C and the 13 °C isotherms are denoted by thick black lines. Timings of the UCTD observations on NLIWs are remarked with gray vertical lines, and maximum and minimum isotherm depths observed from the UCTD (same as shown in Figure 4) displaced by the NLIWs are indicated with red squares and circles, respectively, whereas the maximum isotherm depths observed from the VLA-1 displaced by the NLIWs are indicated with red triangles in (a)–(c). White squares on the left axes denote depths of thermistors attached to the VLAs.

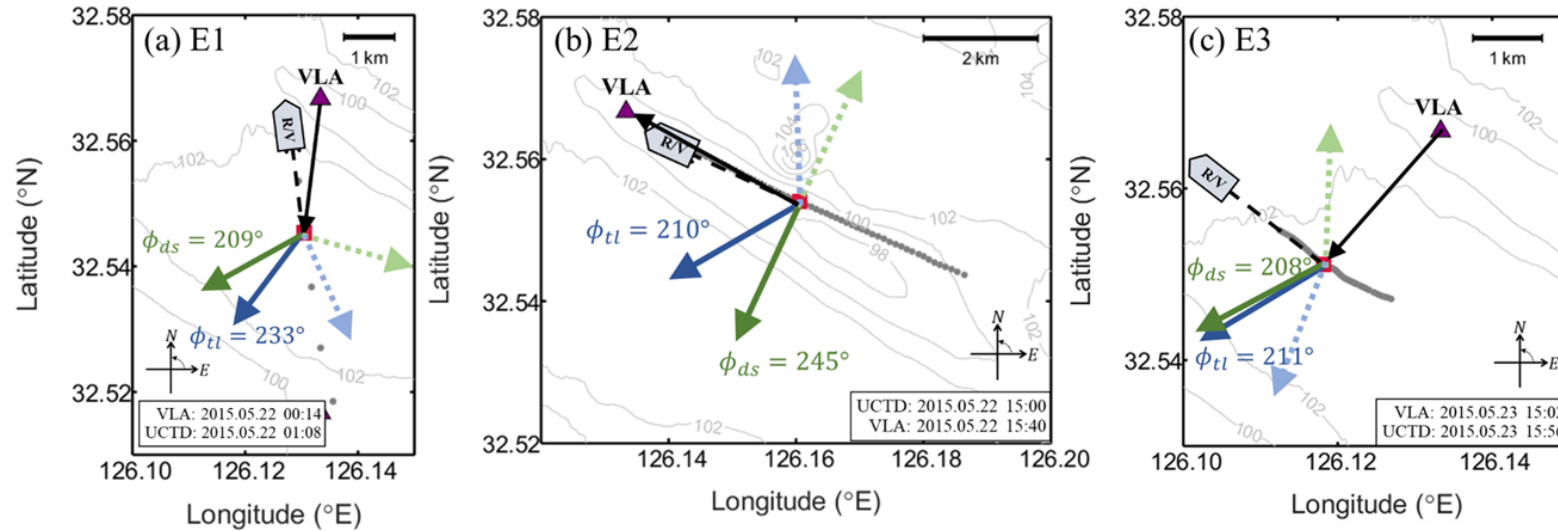


Figure 3.4. Schematics showing propagation direction of NLIWs observed during the events of (a) E1, (b) E2, and (c) E3, estimated from the Doppler shift method (green arrows) and the time lag method (blue arrows) where the propagation directions used to yield the optimal propagation direction are shown with thick solid arrows (others not used are marked as thick dashed arrows). The ϕ_{sh} , ϕ_{obs} , θ_{ds} , and θ_{tl} are labelled in the plots. Date and times of the corresponding events are noted in the bottom corners.

Table 3.1. Observed, calculated, and estimated parameters of nonlinear internal waves (NLIWs) for the three events (E1, E2, and E3).

Parameters		E1	E2	E3
Observation				
ρ_1 (kg m ⁻³)	Upper layer density	1023.44	1023.36	1023.35
ρ_2 (kg m ⁻³)	Lower layer density	1025.16	1025.16	1025.17
h_1 (m)	Upper layer thickness	39.6	35.2	34.8
h_2 (m)	Lower layer thickness	60.4	64.8	65.2
η_0 (m)	Wave amplitude	-4.2	-5.3	-6.1
T_{ap} (sec)	Wave apparent period	575	1291	1695
ϕ_{sh} (°)	Ship course	97	155	148
v_{sh} (m s ⁻¹)	Ship speed	3.28	1.02	0.47
T_{obs} (sec)	Time lag between two different observations	3213	2234	3239
D_{obs} (m)	Distance between two different observations	2383	2814	2233
C_{obs} (m s ⁻¹)	Speed between two different observations	0.74	1.26	0.69
ϕ_{obs} (°)	Angle between two different observations	263	151	230
Estimation based on KdV model				
α (s ⁻¹)	Nonlinear parameter	-0.0082	-0.0122	-0.0127
β (m ³ s ⁻¹)	Dispersion parameter	250	238	238
c_l (m s ⁻¹)	Linear phase speed	0.63	0.63	0.63
c_{iw} (m s ⁻¹)	Propagating speed based on KdV theory	0.64	0.65	0.65
Δ_{iw} (m)	Characteristic width based on KdV theory	592	451	384
λ_{iw} (m)	Wavelength based on KdV theory	1098	836	712
Estimation based on Lee and Nam (2021)				
θ_{ds} (°)	Angle between ϕ_{ds} and ϕ_{sh}	113	90	60
ϕ_{ds} (°)	NLIW propagation direction from Doppler shift	209	245	208
θ_{tl} (°)	Angle between ϕ_{tl} and ϕ_{obs}	30	59	19
ϕ_{tl} (°)	NLIW propagation direction from time lag	233	210	211
c_{iw} (°)	Optimal NLIW propagating speed	0.57	0.73	0.64
ϕ_{iw} (°)	Optimal NLIW propagating direction	212	222	210

Five groups of NLIWs (waves a–e in Figure 3.1) were observed at VLA1 with a time interval 24–96 min shorter than the canonical semidiurnal period (12.42 h; M2), indicating that the phase was not exactly locked to semidiurnal barotropic tides (Figure 3.1 and Table 3.2). The differences in arrival time from wave a to wave e with reference to the M2 phase were 24, 72, 96, and 91 min, and the NLIWs were observed at VLA1 and VLA2 during, or a couple of days after, the spring tides, corresponding to the first half of SAVEX15, and not the remaining half (Figure 3.5a). In contrast to the NLIWs observed from UCTD at a specific phase of the M2 cycle ($\sim 75^\circ$, x in Figure 3.5b), those observed at VLA1 were markedly unlocked to the M2 phase of barotropic tides.

Table 3.2. Applications of the two layered Korteweg-deVries (KdV) and empirical models to the northern East China Sea (ECS) for May 2015. (Top) Daily binned, propagation speed (V) at VLA1 estimated from the KdV model and wave speed parameter (A) of the empirical model. (Bottom) Differences in arrival time and corresponding M2 tidal phase of three types (Type-A, -B, and -C waves) of NLIWs at VLA1 (waves a–e), for both observed and modelled waves (generated in sites i), ii), and iii), respectively). Numbers in parentheses denote difference from the observations.

Date(mm/dd)	05/15	05/16	05/17	05/18	05/19	05/20	05/21	05/22	05/23	05/24
V (m/s)	0.575	0.580	0.585	0.590	0.595	0.600	0.613	0.624	0.635	0.645
A (m/s)	2.065	2.080	2.095	2.110	2.125	2.145	2.200	2.240	2.280	2.310
	wave-a	wave-b	wave-c	wave-d	wave-e					
<i>Arrival time difference (min) at VLA1 referenced to M₂ phase, set to zero for wave-a</i>										
Observed waves	0	-24	-72	-96	-91					
Type-A waves	0	-53 (29)	-74 (2)	-90 (6)	-101 (10)					
Type-B waves	0	-44 (20)	-66 (6)	-82 (14)	-90 (1)					
Type-C waves	0	-11 (13)	-30 (42)	-21 (75)	-80 (11)					
<i>Arrival phase difference (degree) at VLA1</i>										
Observed waves	191	180	145	98	55					
Type-A waves	191 (0)	165 (15)	129 (16)	86 (13)	37 (18)					
Type-B waves	191 (0)	170 (10)	138 (7)	98 (0)	54 (1)					
Type-C waves	96 (95)	100 (80)	76 (69)	80 (18)	27 (28)					

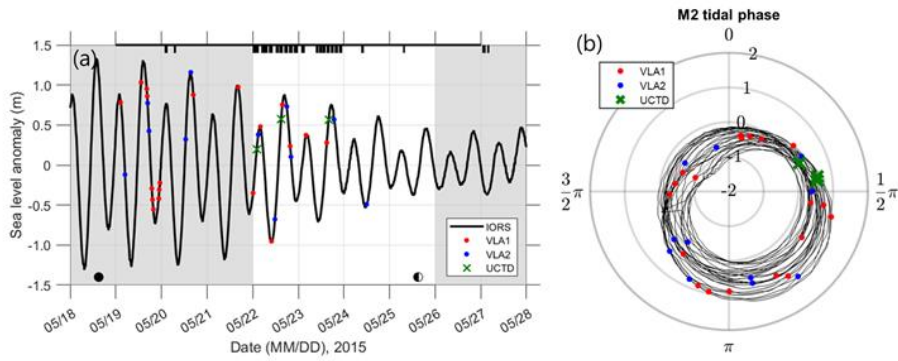


Figure 3.5. (a) Time series and (b) M2 tidal phase of sea level anomaly (solid black lines) observed at the IORS where timings of NLIWs observed at VLA1, VLA2, and UCTD are marked with red and blue dots and green crosses. In (a) and (b), the y-axis and radial axis represent sea level anomalies. The periods of spring and neap tides are denoted by gray and white areas, respectively, in (a). Timings of the UCTD profiling are noted with thick black tick markers on the top x-axis in (a), and total measurement periods of VLAs are denoted with a thick black horizontal line on the top x-axis.

The surface manifestations of NLIWs observed from 93 MODIS images from 2015 to 2019 indicate at least three different sources of NLIWs in the northern ECS based on the curvatures (Figure 3.6). The number of NLIWs in a group generally increased as they propagated from the three potential generation sites: i) northern Okinawa Trough (Type-A, orange), ii) western Fukue Island (Type-B, blue), and iii) southwestern Jeju Island (Type-C, green). For example, 5 groups of Type-A NLIWs (waves #1 to #5; orange in Figure 3.6a) were found in one image (taken in July 20, 2018) among a total of 58% (54 among 93) of MODIS images with a distance (wavelength of semidiurnal internal tides) ranging from 41 to 53 km, indicative of corresponding propagation speeds of semidiurnal internal tides ranging from 0.91 to 1.18 m s⁻¹ (with the fixed M2 period). Similar, but with slightly different patterns, were three groups of Type-B NLIWs (waves #1 to #3; blue in Figure 3.6a) with a distance ranging from 48 to 63 km (1.07 to 1.41 m s⁻¹ in propagation speed) and other groups of Type-C NLIWs (green in Figure 3.6a) that were observed in the same image among 46% (43 of 93) and 25% (23 of 93) of MODIS images.

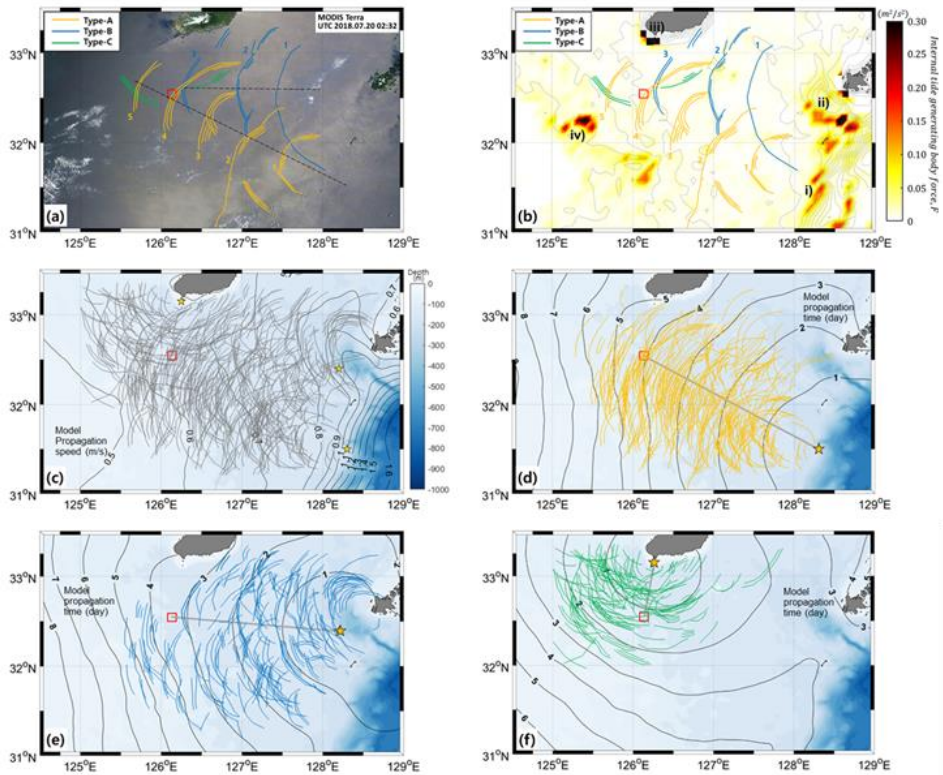


Figure 3.6. (a) Satellite MODIS Terra image taken in the northern ECS at 02:32 UTC on 20 July 2018 where surface manifestations of three types (Type-A; yellow, Type-B; blue, and Type-C; green) of NLIWs are identified. (b) Map of maximum depth-integrated M2 internal tide-generating body force in $\text{m}^2 \text{s}^{-2}$ derived from buoyancy frequency from the WOA18 data, where the surface patterns of three types of NLIWs propagating from three potential generation sites i), ii), and iii) are superimposed on the bathymetry (thin gray contours). Surface manifestations of (c) all (gray), (d) Type-A (yellow), (e) Type-B (blue), and (f) Type-C (green) NLIWs identified from 93 MODIS images, superimposed on bathymetry (blue colors) and wave fronts (black contours labelled with model propagation time in day) estimated using the empirical model (Jackson, 2009) with a wave speed parameter $A = 2.4 \text{ m s}^{-1}$. Minimum distances between the generation sites (yellow stars) and the SAVEX15 area (red boxes) are marked with thick gray lines in (d), (e), and (f).

3.1.2. Modeled NLIWs

The propagation speed of mode-1 NLIWs modeled by the two-layered KdV theory was nearly the same (0.64, 0.65, and 0.65 m s⁻¹) during the three events of NLIWs observed from the UCTD observations on May 22–23, 2015 (E1, E2, and E3; Table 3.1), whereas the propagation speed calculated using the time-varying stratification parameters from the VLA observations showed markedly increasing trends at VLA1 and VLA2 during the SAVEX15 experiment (Figures 3.7 and 3.8). The increasing trend in propagation speed was primarily due to decreasing (increasing) trends in the upper layer density ρ_1 (temperature t_1). The increase in t_1 and decrease in ρ_1 resulted in an increase in the difference between the temperature (Δt) and density ($\Delta\rho$) between the layers, increasing c_{iw} .

The propagation speed of mode-1 NLIWs modeled by the KdV theory is consistent with that of the empirical model at the corresponding water depth. The wave speed parameter A in Equation (2.11) was determined to be 2.4 m s⁻¹ for the SAVEX15, which is higher than that (2.0 m s⁻¹) derived from the historical data collected in May (Figure 2.5). Spatial patterns of propagating NLIWs from the three potential generation sites i), ii), and iii), modeled by the empirical model using bathymetry, reasonably explain the surface manifestations of the three types (Type-A, Type-B, and Type-C) of NLIWs observed from the MODIS images (Figure 3.6). The Type-A, Type-B, and Type-C NLIWs are modeled to arrive in the SAVEX15 area in 4.11, 3.39, and 1.14 days, when propagating from site i), ii), and iii), respectively (Figure 3.6d-f).

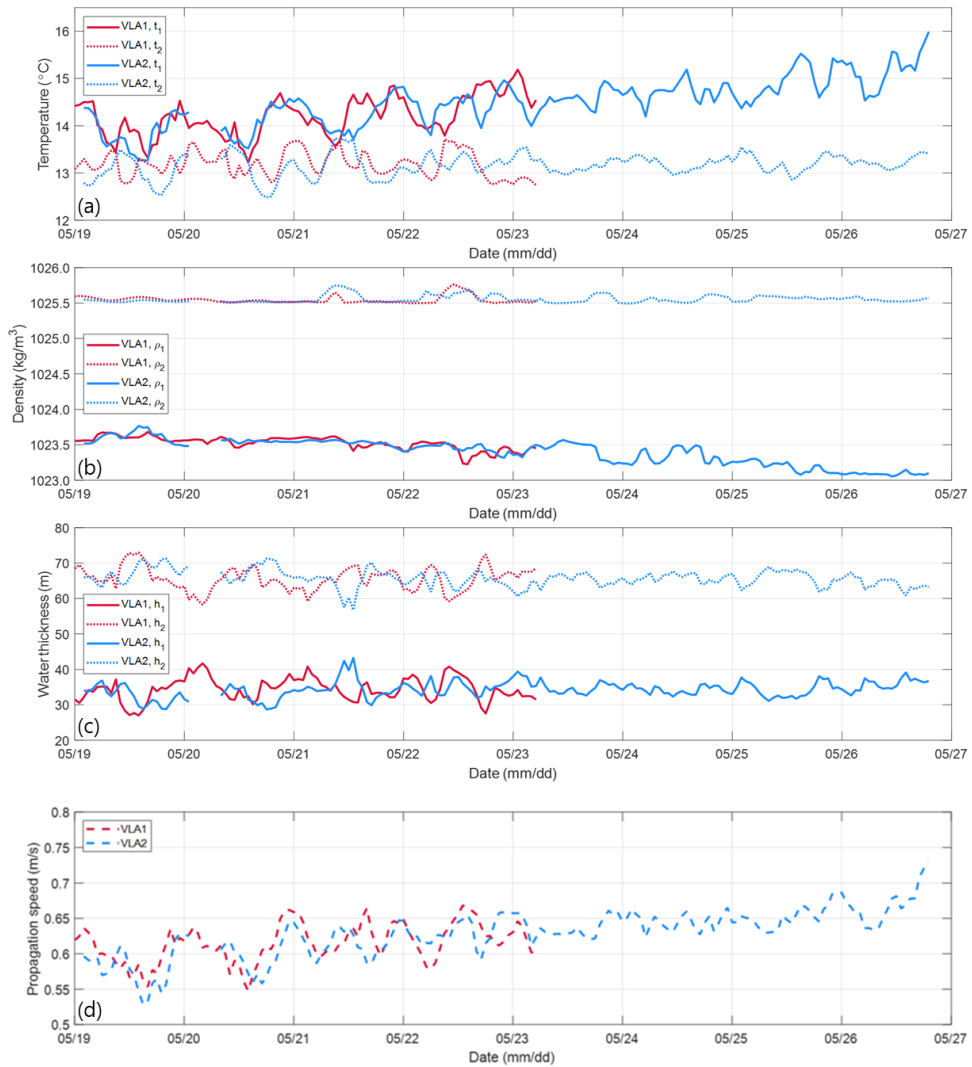


Figure 3.7. Time series of hourly binned (a) upper (t_1 , solid lines) and lower (t_2 , dashed lines) layer temperatures, (b) upper (ρ_1 , solid lines) and lower (ρ_2 , dashed lines) layer densities, (c) upper (h_1 , solid lines) and lower (h_2 , dashed lines) layer thicknesses at VLA1 (red) and VLA2 (blue), and (d) propagation speed at VLA1 (red dashed line) and VLA2 (blue dashed line).

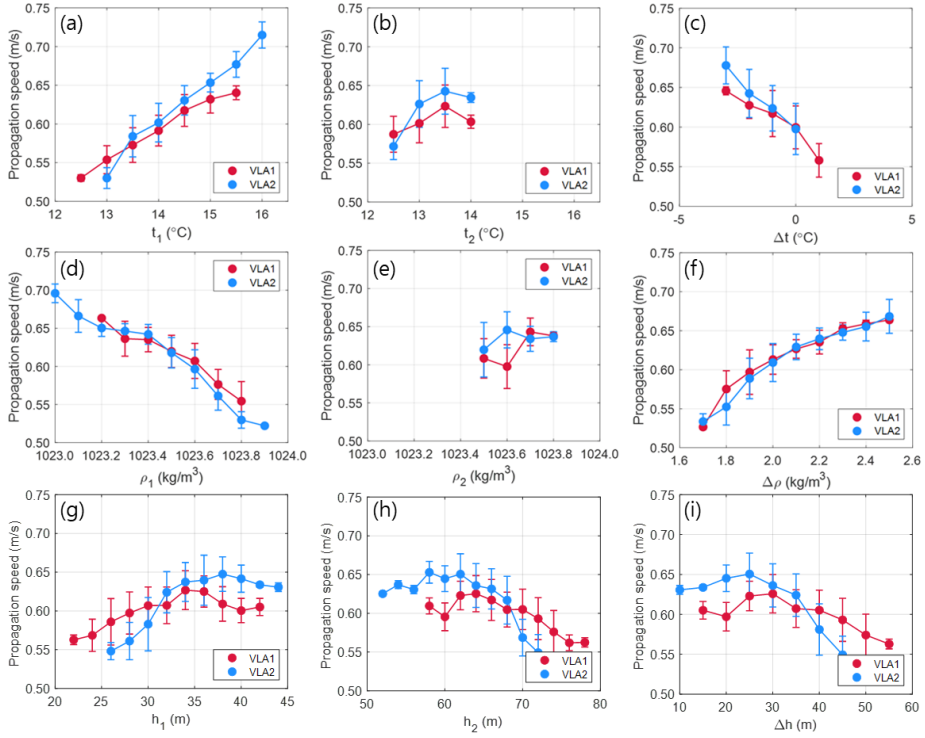


Figure 3.8. The propagation speeds of NLIWs are shown as functions of (a) t_1 , (b) t_2 , and (c) temperature difference ($t_2 - t_1$), (d) ρ_1 , (e) ρ_2 , and (f) density difference ($\rho_2 - \rho_1$), and (g) h_1 , (h) h_2 , and (i) layer thick difference ($h_2 - h_1$) at VLA1 (red) and VLA2 (blue). In (d)–(i), the binned mean and one standard deviation from the mean are denoted with colored circles and vertical bars, respectively.

3.1.3. Seasonal variation

The amplitude, propagation speed, and characteristic width of the NLIWs observed in the SAVEX15 area during May 2015 were compared to those previously investigated. The typical amplitudes, propagation speed, and characteristic width of NLIWs in the region, identified only for summer previously, ranged from 3 to 10 m, 0.9 to 1.1 m s⁻¹, and ~200 m, respectively (Lee et al., 2006; Lozovatsky et al., 2015; Smith, 2010; Teixeira et al., 2006). The spring NLIWs observed during E1, E2, and E3 have significantly longer widths and lower propagation speeds than those previously identified in the region for summer, although the amplitudes were within a similar range (Figure 3.9). As the KdV model predicts, and Cho et al. (2016) confirmed using historical hydrographic data collected over the past decades, the characteristic width and propagation speed of mode-1 NLIWs depend on stratification parameters that vary markedly over seasons in the region. The springtime (May) NLIWs presented in this study have relatively longer width and lower propagation speed due to higher density (lower temperature) in the upper layer (e.g., high ρ_1 (low t_1) with no significant difference in lower layer density (temperature), yielding smaller vertical density (temperature) differences between the layers ($\Delta\rho$ (Δt)), smaller amplitudes of c_l , α , and β , and ultimately smaller c_{iw} and longer Δ_{iw} for a given amplitude (Equations (2.6) and (2.7), and Figures 3.7 and 3.8), compared to stratification and KdV parameters in summer (Cho et al., 2016).

Although springtime NLIWs have not been directly observed in the region, the characteristic width and propagation speed of the May NLIWs observed in 2015 were compared with the May climatology of mode-1 NLIWs in the region (Cho et al., 2016). Interestingly, the characteristic width and propagation speed of NLIWs

observed during the events of E1, E2, and E3 in 2015 were 150–300 m longer and 0.2 m s^{-1} higher than those predicted by the climatology in Cho et al. (2016) for the given amplitude (Figure 3.9). Such faster-than-normal propagation with longer-than-normal width of NLIWs in May 2015 is due to the somewhat abnormal stratification of the year. In May 2015, the thermocline was deeper, yielding a thicker upper layer ($h_1=35 \text{ m}$), and the stratification was enhanced, yielding lower density in the upper layer ($\rho_1=1023.53 \text{ kg m}^{-3}$), compared to the climatological condition ($h_1=23 \text{ m}$ and $\rho_1=1024.62 \text{ kg m}^{-3}$).

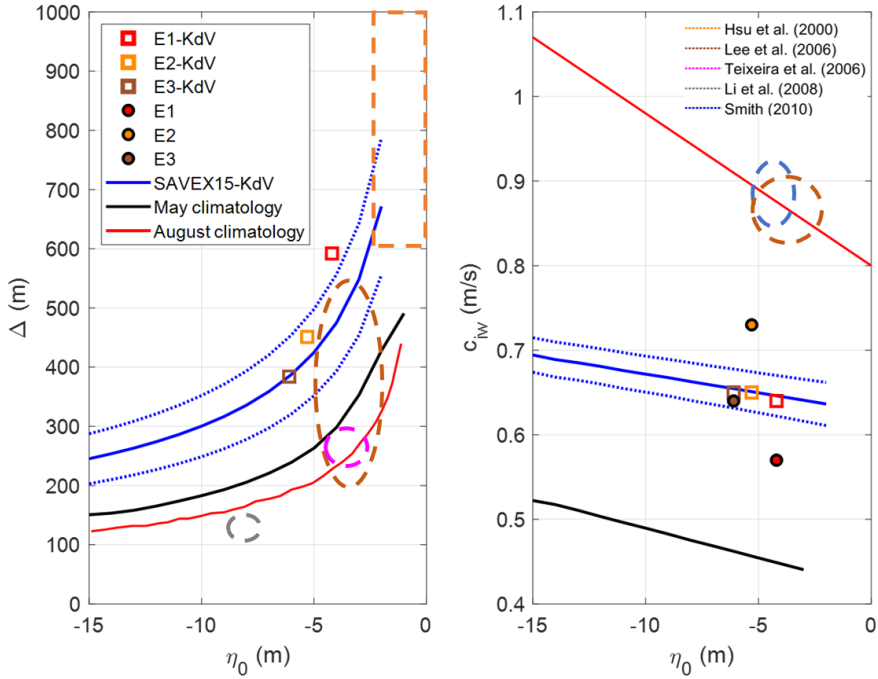


Figure 3.9. (a) Characteristic width and (b) propagation speed of NLIWs as a function of the wave amplitude η_0 obtained using the two layered KdV model from the historical hydrographic NIFS data collected in May, or May climatology (black solid lines, same as presented in Cho et al., 2016) and SAVEX15 VLAs data collected in May 2015 (blue solid lines), where the standard deviations from the mean are denoted with black and blue dotted lines, respectively. Characteristic width and propagation speed of NLIWs during the events of E1, E2, and E3 obtained using the two layered KdV model from the SAVEX UCTD data (open squares) and optimal approach presented in Lee and Nam (2021) using the Doppler shift method and time lag method (filled circles) are compared.

To discuss seasonal variation of propagation of NLIWs, the propagation speed of NLIWs as the function of the water depth in northern East China Sea are calculated using two-layered KdV model and empirical model (Figure 3.10). In winter (January, February, and March; red solid line in Figure 3.10), the propagation speed is similar to the empirical model (parameter $A = 0.5$) and increases with deeper water depth. A variation of propagation speed (red shaded) is smaller than others season, but the stratification of the water column becomes very weak or disappears completely such that no NLIWs can exist (Alpers et al., 2005). In spring (April, May, and June; blue solid line in Figure 3.10), the propagation speed is well matched the empirical model (parameter $A = 2.0$) and increases with deeper water depth. In summer (July, August, and September; yellow solid line in Figure 3.10), the propagation speed becomes slower than the empirical model (between parameter $A=3.5$ and 4.0) as the depth is deeper. In contrary, in Fall (October, November, and December; green solid line in Figure 3.10), the propagation speed becomes faster than the empirical model (between parameter $A=1.5$ and 2.5) as the depth is deeper.

Spatial seasonal variation of propagation speed of NLIWs is also significant. In spring, the propagation speed in east area in northern ECS is faster than them in other area in northern ECS due to the difference in water thickness of the upper and lower layers (Figure 3.11). In summer, the propagation speed in east and north area in northern ECS is faster due to stratification. Since difference density between upper and lower layers in northwest have strong stratification, the propagation speed is fast. In fall, the low propagation speed has due to weak stratification (Figure 3.11).

The propagation speed of NLIWs in northern ECS increases as the depth of the water increases, regardless of the season, yielding well matched empirical model with given parameters A . Seasonal variations of propagation speed from KdV model

using historically climatology data are significant. The propagation speed in summer is fast, in contrast the speed in winter is slow due to stratification. In this area, observed and model based propagating speed are similar, these means model-based propagation speed is significant.

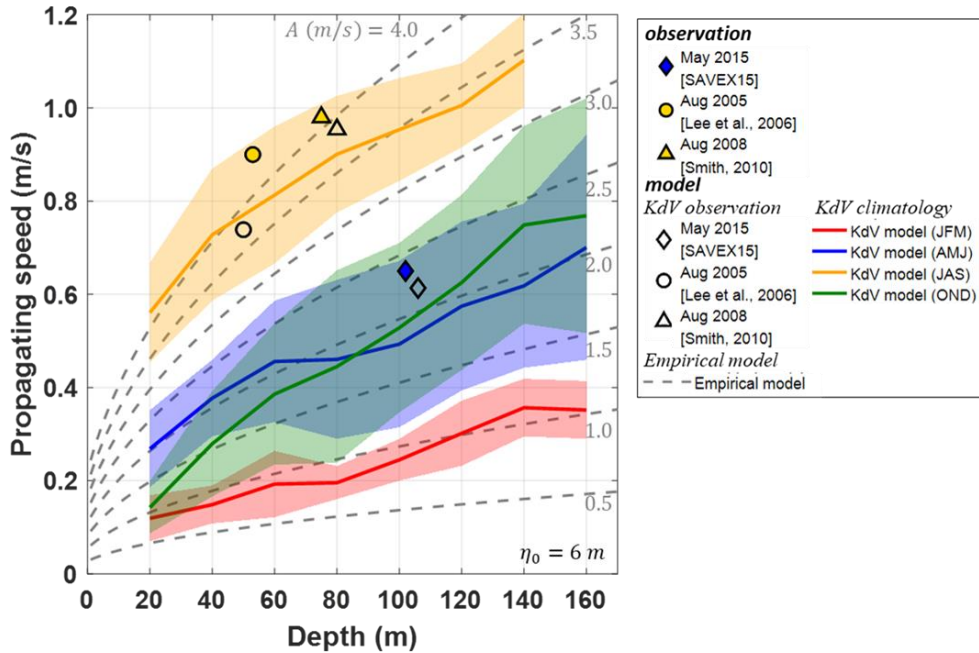


Figure 3.10. Propagation speed of NLIWs as function of water depth in northeastern East China Sea. The open and color markers mean propagation speed of NLIW each season from model and in-situ observation. The color solid lines mean historical climatology data, which is calculated two-layered KdV model at an amplitude of 6 m, with interval of 20 m as derived from the NIFS/KODC data (red: January, February, and March; blue: April, May, and June; yellow: July, August, and September; green: October, November, and December). The shaded area means one standard derivation. The gray dashed line means modified A parameters of empirical model (Equation 2.11).

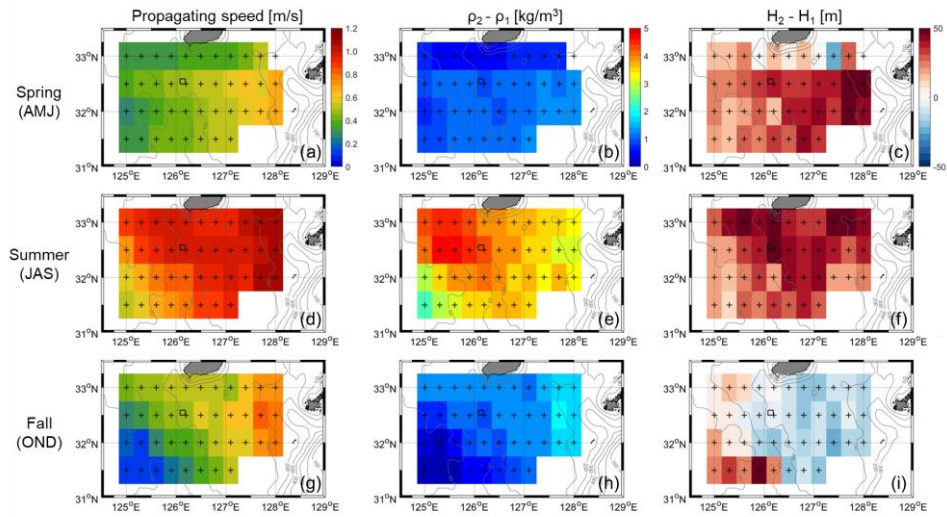


Figure 3.11. Seasonal spatial map of (a, d, g) propagation speed of NLIWs, (b, e, h) difference of density between upper layer and lower layer density, and (c, f, i) difference of water thickness between upper layer and lower layer in spring (a-c), summer (d-f), and fall (g-i). The historical hydrographic data from NIFS KODC denote black cross markers. The black box denotes the SAVEX15 area.

3.2. Generation of NLIWs in the northern ECS

There are four potential generation sites of NLIWs in the northern ECS, identified using the depth-integrated, internal tide-generating body force F , following Baines (1982), a term often used to identify internal wave hotspots (Li et al., 2008; Niwa and Hibiya, 2004; Shen et al., 2019).

$$F = -\frac{\vec{Q}\nabla H}{\omega H^2} \int_{-H}^0 zN^2(z)dz \quad (3.1)$$

Here, ω is the tidal angular frequency (rad s^{-1}), which is fixed to the M2 frequency, z is the vertical coordinate ($z = 0$ at the sea surface, upward positive), $N(z)$ is the local buoyancy frequency, Q is the barotropic tidal transport $Q = (Q_x, Q_x) = (uH, vH)$, u and v are the zonal and meridional components of the barotropic tidal current, and H is the local water depth (Figure 3.12). Strong body force is localized at four sites in the northern ECS: i) northern Okinawa trough, ii) western Fukue Island, iii) southwestern Jeju Island, and iv) near the IORS (Figures 3.12 and 3.13). Although NLIWs generated from site iv) have been reported previously (Nam et al., 2018), those from the three other sites have not previously been identified, and only site i) has been suggested as a potential generating site for NLIWs observed in the vicinity of IORS (Lee et al., 2006).

The NLIWs observed in the SAVEX15 area, located in the middle of the generating sites, might be generated from either one or multiple sites and may propagate in multiple directions passing through the area. The spatial patterns of surface manifestation of groups of NLIWs observed via MODIS images support the fact that one or a couple of NLIWs in a group are accompanied by the northwestward (Type-A waves), westward (Type-B waves), and southward (Type-C) propagating

semidiurnal internal tides generated from site i), ii), and iii), respectively, for at least a few days (1.14 to 4.11 days) with a propagation speed ($0.91\text{--}1.18\text{ m s}^{-1}$) higher than the propagation speed ($0.57\text{--}0.73\text{ m s}^{-1}$) of NLIWs observed in the shallow SAVEX15 area. The NLIWs observed in the SAVEX15 area may not be generated locally, but may instead be remotely generated, as supported by:

1. A relatively flat bottom in the SAVEX15 area with weak body force (Figure 3.13);
2. A time interval departed from the M2 tidal cycle period of groups of NLIWs (waves a–e) observed at VLA1 (Figure 3.1, left); and
3. NLIWs were observed at VLAs during, or a couple of days after, the spring tides (Figure 3.5a).

To discuss timing of M2 tide at four potential generation sites of NLIWs in the northern ECS identified using horizontal barotropic tidal energy flux for M2 constituent (Niwa and Hibiya, 2004).

$$E = \rho g Q \zeta \text{ [W/m]} \quad (3.2)$$

Here, ρ is depth-averaged density (kg m^{-3}) from WOA18 data, g is the gravity acceleration (m s^{-2}), Q is barotropic tidal transport ($\text{m}^2 \text{s}^{-1}$), and ζ is surface tidal elevation (m). The half of M2 phase is divided five stages (a–e; Figure 3.14) at SAVEX15. Strong horizontal barotropic tidal energy flux in stage a and e is localized at generation site i) and iv). Other strong horizontal barotropic tidal energy flux in stage e (or c) is localized at generation site ii) and ii).

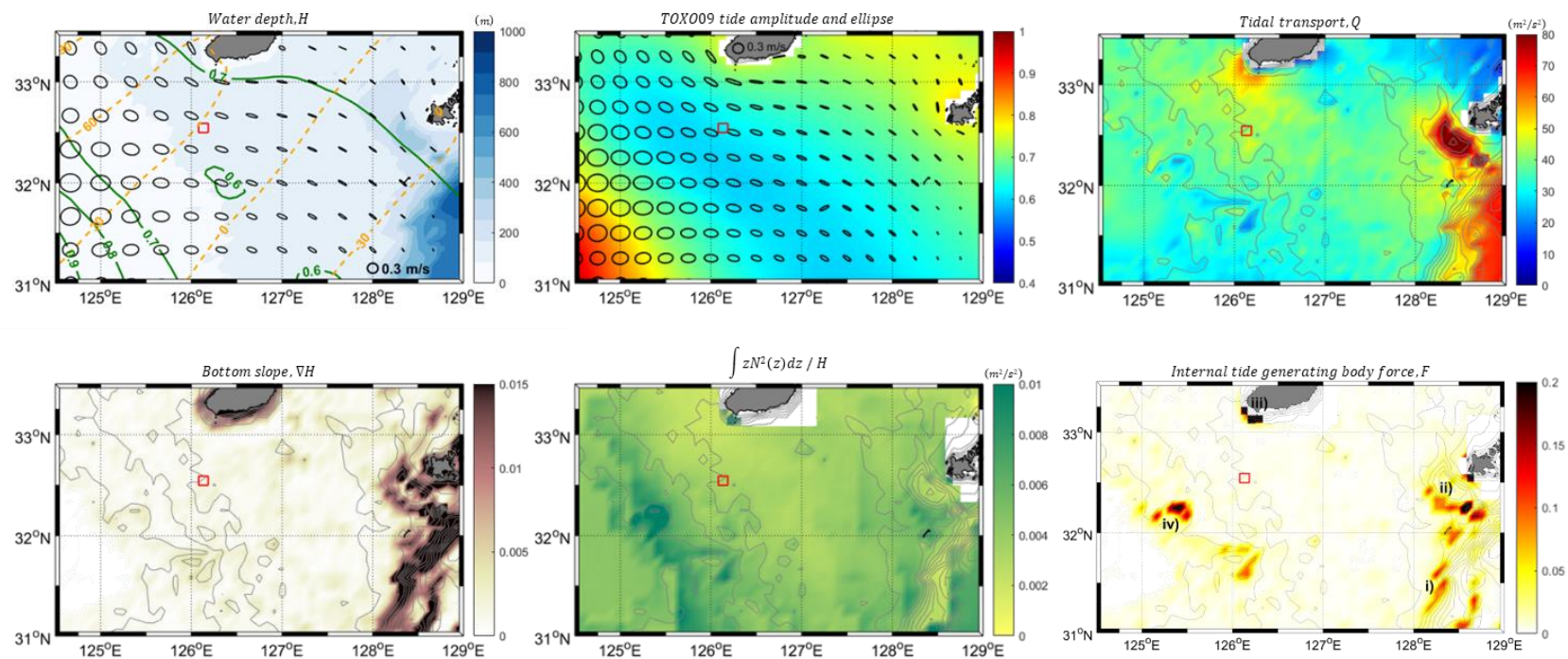


Figure 3.12. Water depth, tide amplitude and phase, tidal transport, bottom slope, depth-normalized buoyancy frequency, and internal tide generating body force.

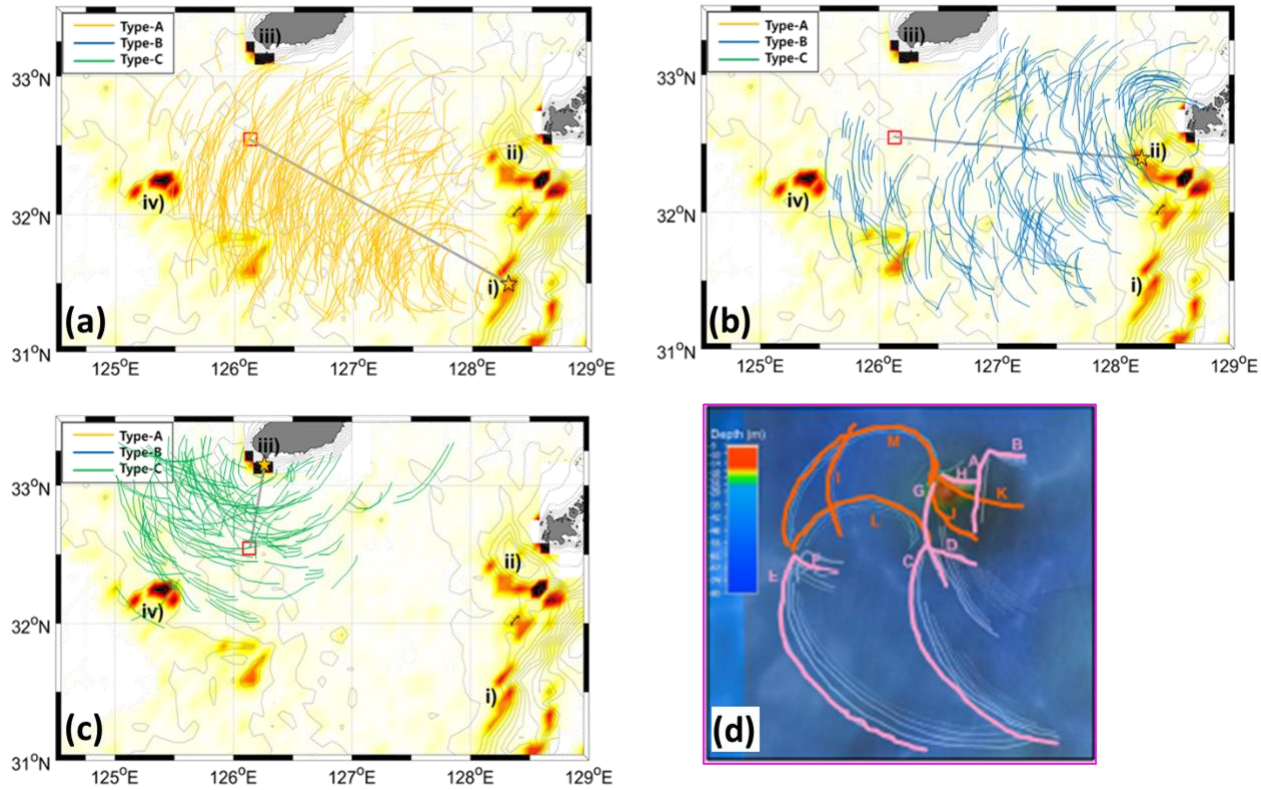


Figure 3.13. Map of maximum depth-integrated M2 internal tide-generating body force in $\text{m}^2 \text{s}^{-2}$ derived from buoyancy frequency from the WOA18 data, where the surface patterns of three types of NLIWs (i, ii, and iii) propagating from four potential generation sites (a-d). The (d) images is from Nam et al., (2018).

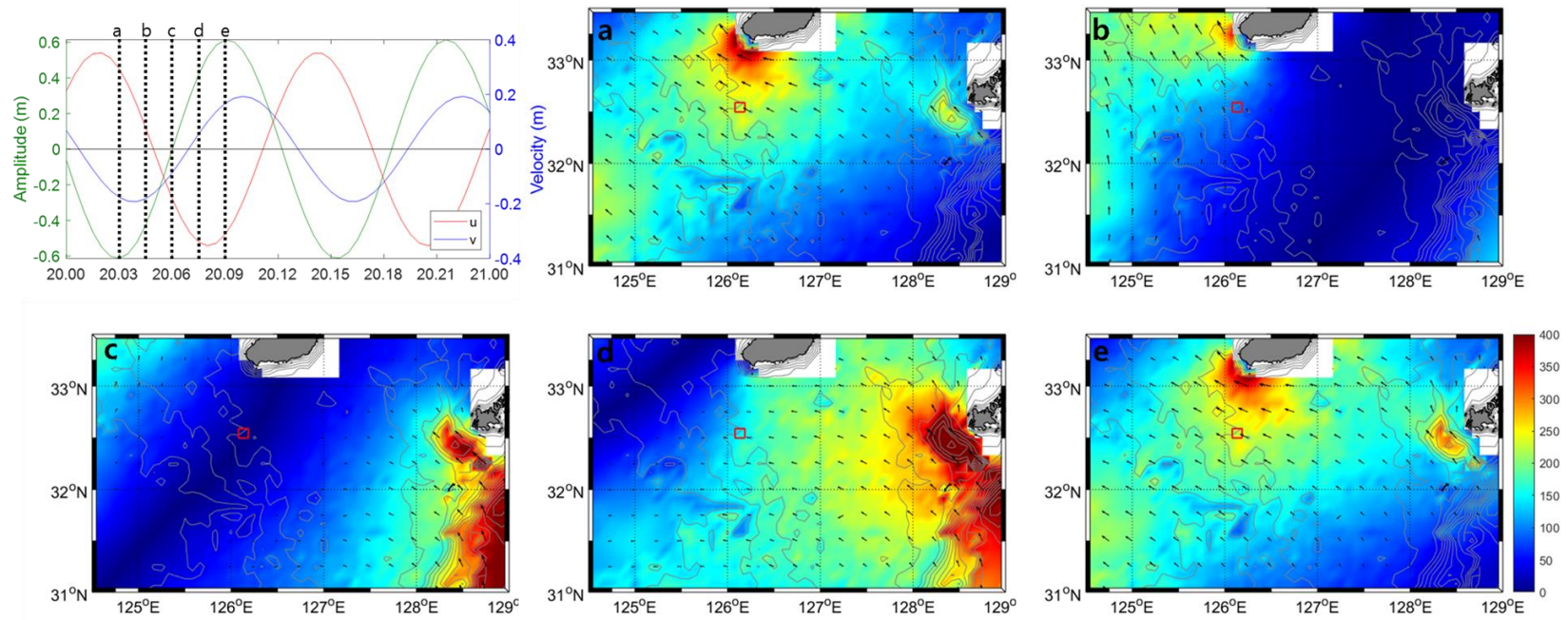


Figure 3.14. Map of horizontal barotropic tidal energy flux (W m^{-1}) for M2 constituent derived from the WOA18 data in five stages (a-e).

3.3. Propagation of NLIWs from the generation sites

To calculate the propagation time from the empirical model (Equation 2.11), it is necessary to specify a geographically generation site for the waves. The four locations can be additional model parameters that are derived from the satellite observation and depth-integrated body force. With the model parameters established and thus the ability to determine the propagation time to any location in the region of interest, the empirical model can serve as the basis for a prediction system. Arrival time predictions can be made for fixed locations or propagation time contours produced at intervals based on the generation relationship to the tidal cycle can be used to create wave front location maps (Figures 3.13).

The NLIWs observed at VLA1 in the SAVEX15 area were examined from the perspective of Type-A, Type-B, and Type-C NLIWs accompanied by the semidiurnal internal tides generated from the three sites i), ii), and iii) using spatiotemporally varying propagation speeds derived from the empirical model (Equation 2.11) and VLA1 observations of waves a–e (Figure 3.15). The time-varying propagation speed of NLIWs at VLA1 (Figure 3.15a) was extended to the speed as a function of water depth and time using Equation (2.11) (Figure 3.15b) and ultimately to the spatiotemporally varying propagation speeds between VLA1 and each generation site for the Type-A, Type-B, and Type-C waves (Figures 3.15c–3.15h). The resultant arrival times and M2 phases of Type-A and Type-B waves agree with those observed at VLA1 (within 30 min in time and 20° in phases). In contrast, Type-C waves markedly (maximum 75 min in time and 96° in phases) depart from the observations (Figure 3.15i and Table 3.2). Along with the consistent time intervals of waves a–e observed at VLA1, the propagation direction (southwestward) observed during the

E1, E2, and E3 events are more consistent with the westward-propagating Type-B waves than with the northwestward-propagating Type-A waves (Figure 3.6).

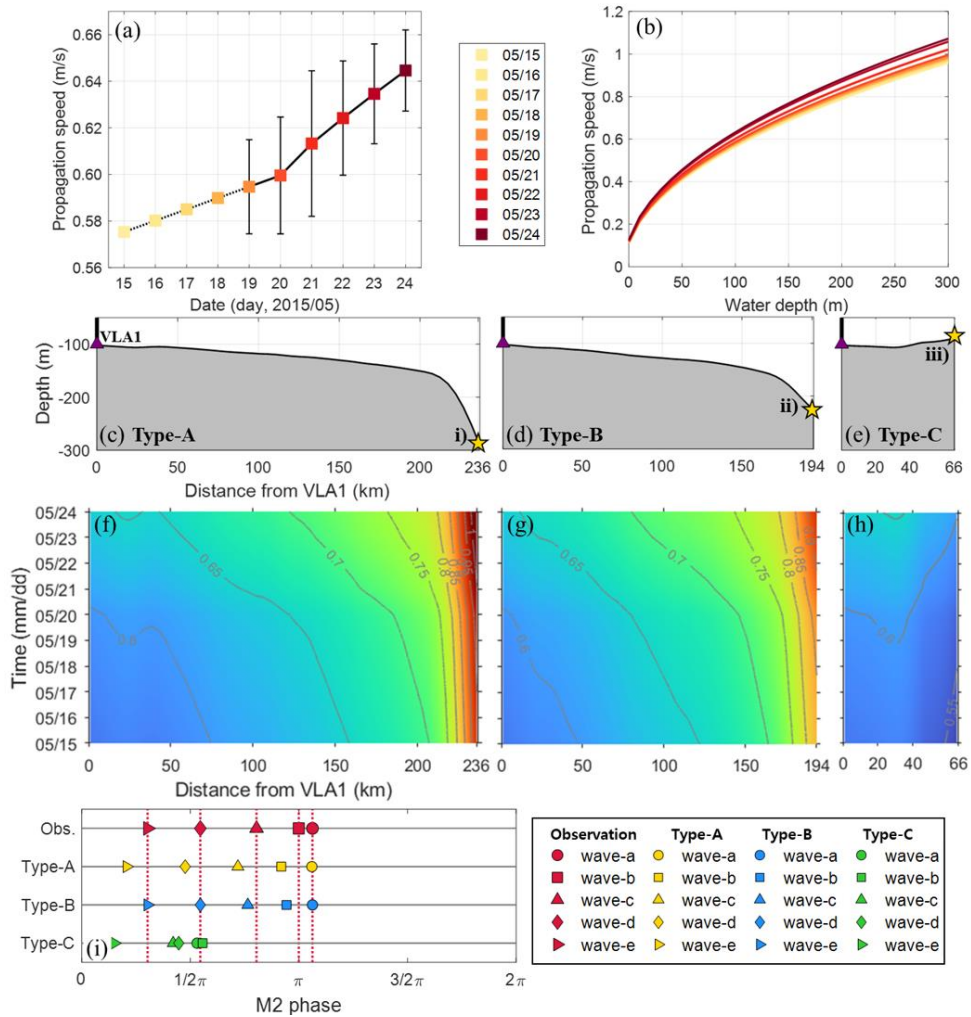


Figure 3.15. (a) Time series of daily binned propagation speed of NLIWs (colored squares) estimated from VLAs data with its standard deviations (vertical bars) and (b) daily profiles of propagation speed of NLIWs as a function of water depth estimated using the empirical model by fitting to the daily variations of propagation speed at VLA1. In (a), the propagation speeds in May 15–18 were obtained by linearly extrapolating the speeds in May 19 and 20. Water depth profiles along the lines (shown in Figure 3.6d, 3.6e, and 3.6f with thick gray lines) between the VLA1 and generation sites i), ii), and iii) (yellow stars) for (c) Type-A, (d) Type-B, and (e) Type-C NLIWs. Time–distance contours of propagation speed of (f) Type-A, (g) Type-B, and (h) Type-C NLIWs with labels in m s^{-1} . Timings of the arrival of observed (red, shown in Figure 3.1 left), Type-A (yellow), Type-B (blue), and Type-C (green) waves a–e in VLA1 as a function of M2 phase.

3.4. Limitation of KdV models

The two-layered classical (ordinary) KdV theory used in this study has clear limitations. The classical KdV theory is very simplified and assumes weak non-linearity and weak dispersiveness. In fact, NLIWs observed in many areas have been better explained by the eKdV theory than by the KdV theory. However, propagation speeds, in cases of SAVEX15 and IORS18, derived based on the eKdV theory ($c_{eKdV.iw}$) including the cubic non-linearity are not significantly different from those based on the KdV theory ($c_{KdV.iw}$), yielding the difference less than 0.02 m s^{-1} due to relatively small η_0 (Table 2.1). The theoretical propagation speeds in the forms of Equations (2.6) and (2.9) are limited to the case of no background pedestal condition that could not be considered in this study and might affect the speed significantly. In addition, the results presented in this study are limited to only mode-1 NLIWs by applying the two-layered system, yet the vertical profiles of mean density observed during the two experiments (Figures 2.9b and 2.12b) support normal mode decompositions (J. Klinck's Matlab program `dynmodes.m`) for the first three modes corresponding to 49%, 18%, and 14% for SAVEX15 and 50%, 21%, and 13% for IORS18, respectively. Multi-mode NLIWs beyond the mode-1 NLIWs in the region, yet explaining about half of NLIWs, need to be examined in the future.

Furthermore, as in the case of NLIWs in the South China Sea, finite-depth theory may be theoretically more appropriate than shallow-water theory where the KdV and eKdV theories are based on Cai et al. (2013). To understand the characteristic parameters of NLIWs, three regimes of weakly NLIW theories have been developed, including shallow-water, deep-water, and finite-depth and underlying scaling assumptions can be categorized as below.

- Shallow-water theory

$$\frac{\Delta}{H} \gg 1, \frac{h_1}{H} \sim O(1), \frac{\eta_0 \Delta^2}{H^3} \sim O(1)$$

- Deep-water theory

$$\frac{\Delta}{H} \rightarrow 0, \frac{\Delta}{h_1} \gg 1, \frac{\eta_0 \Delta}{h_1^2} \sim O(1)$$

- Finite-depth theory

$$\frac{\Delta}{h_1} \gg 1, \frac{h_1}{H} \ll 1, \frac{\Delta}{H} \sim O(1), \frac{\eta_0 \Delta}{h_1^2} \sim O(1)$$

Herein, considering a broad shelf, the applicability of the methods to shallow-water or finite-depth [Cai et al., 2013]. The observed NLIWs for SAVEX15 have scales of $\eta_0 \sim 6 \text{ m}$, $\Delta \sim 380 \text{ m}$, $h_1 \sim 35 \text{ m}$, and $(H = h_1 + h_2) \sim 100 \text{ m}$, with the associated ratios of $(\Delta/H) \sim 3.80$, $(h_1/H) \sim 0.35$, $(\Delta/h_1) \sim 10.86$, $(\eta_0 \Delta/h_1^2) \sim 1.86$, and $(\eta_0 \Delta^2/H^3) \sim 0.87$, respectively. Based on the above assumptions, the SAVEX15 might be considered shallow-water theory.

The assumption of two-layered system about the stratification structure are also important to propagation speed of KdV model. In this study, the two-layer system was assumed through the minimum and maximum densities of the upper layer and lower layers (red dashed line in Figure 3.16), respectively, in comparison, the averaged upper and lower layer of densities (green dotted line in Figure 3.16) slower 0.11 m/s than the assumption in this study. Furthermore, the real ocean is not a simple two-layered structure, but consist of continuously multilayered structure. In fact, during SAVEX15, the mode-2 NLIWs are observed at generating in at least three-layered structure (Figure 3.17). Multi-mode NLIWs beyond the mode-1 NLIWs in the region need to be examined in the future.

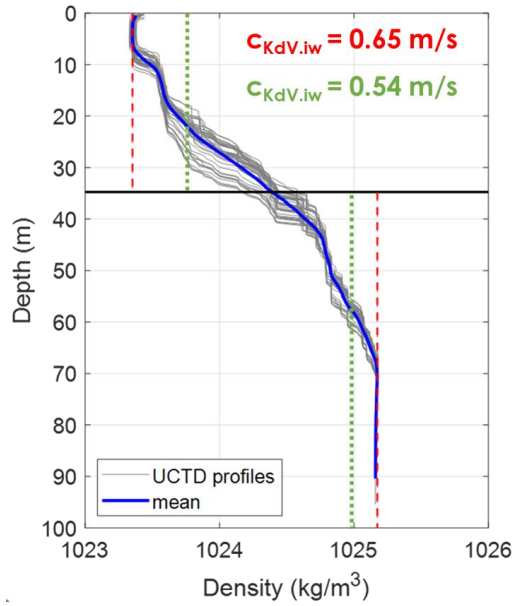


Figure 3.16. The two case of two-layered density structure. The vertical profiles of density obtained from the UCTD measurements (grey) and the average profile (blue). The minimum and maximum densities at the upper and lower layers are shown with red dashed lines and the averaged densities at the upper and lower layers are shown with green dotted lines.

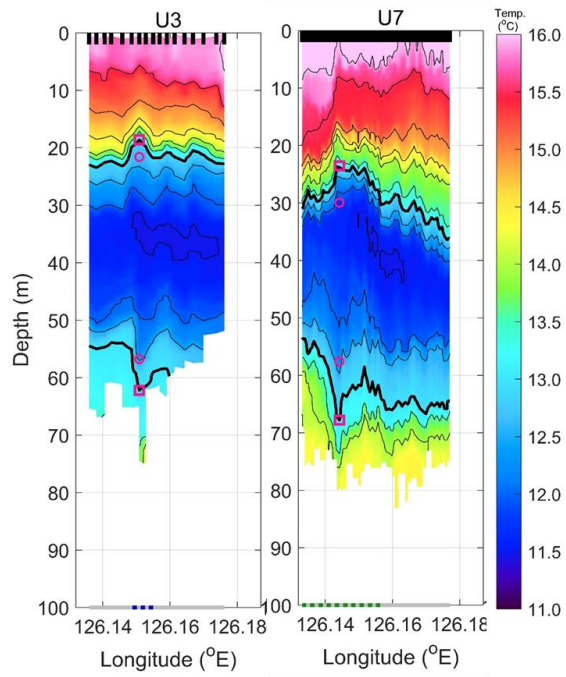


Figure 3.17. Examples of mode-2 NLIWs observed UCTD during SAVEX15

4. Conclusion

Nonlinear internal waves play an important role in regional circulation, biogeochemistry, energetics, vertical mixing, underwater acoustics, marine engineering, and submarine navigation, most commonly generated by the interaction between barotropic tides and bathymetry. In particular, the East China Sea, which is a broad continental shelf with many sources of generation sites and multiple propagated direction, shows different characteristics of NLIWs from neighboring South China Sea and East Sea. So, this study aims to characterize NLIWs observed in spring (May) in the northern ECS based on in-situ observations supplemented by satellite and historical hydrographic data, and to discuss the generation and propagation of mode-1 NLIWs in the region by applying KdV and empirical models.

This study is presented a novel method to estimate the propagation speed and direction of NLIWs using widely collected underway and moored observations, and the results of applying the method to two cases of NLIWs observed in May 2015 (SAVEX15) and August 2018 (IORS18). Two-layered KdV theory and satellite images were used to discuss the results of the proposed method. The propagation direction of NLIWs was estimated with respect to a moving ship using the Doppler shift relationship (1. Doppler shift method) and independently using the time lag between the NLIWs observed at two different locations (2. time lag method). Then, the propagation speed and direction were optimized to minimize the difference in propagation directions derived from the two methods by iterating the propagation speed in the range of $\pm 30\%$ at a resolution of $0.01 \text{ m} \cdot \text{s}^{-1}$. The results derived from the proposed method are robust, as the range of iterative propagation speeds is comparable to the interannual variation of theoretical propagation speeds estimated

using historical hydrographic data, yielding an error of less than 15% for the propagation direction. Because in situ observations of NLIWs are still challenging to collect and propagation speed and direction cannot be directly measured from subsurface instruments, our proposed method for estimating the propagation speed and direction of NLIWs using common underway and moored measurements is of practical importance, particularly over a broad shelf, such as the northern ECS, where the multi-directional propagation of multi-mode NLIWs from multiple sources is often observed.

The NLIWs in the northern ECS were characterized based on moored temperature and ship-based profiling UCTD observations made during the SAVEX15 in May 2015 using the two-layered KdV and empirical models. The observed mode-1 NLIWs had an amplitude of 4–16 m, a characteristic width of 380–600 m, westward and northward propagating directions, and a propagating speed of 0.64–0.72 m s⁻¹. For a given amplitude, the characteristic width of NLIWs identified in spring 2015 in this study is significantly longer than those reported previously for summer and May climatology, whereas the propagation speed of NLIWs is lower than those reported previously for summer, but higher than those for May climatology, which is primarily affected by seasonal and interannual changes in stratification. The climatology in the northern ECS demonstrated that the propagation speed is highest in summer, and seasonal variation of NLIWs is highest in spring and fall. The seasonal variation of propagation speed as function of water depth was due to the stratification difference between the eastern part and the western part. The long-term decreasing trend of propagation speed was observed in May at a rate of $-0.004 \text{ m s}^{-1} \text{ yr}^{-1}$, primarily because of the decreasing density. In contrast, the long-term increasing trend of propagation speed was observed in August at a rate

of $0.003 \text{ m s}^{-1} \text{ yr}^{-1}$ because of the increasing density stratification.

The four major generation sites are suggested in northern ECS using satellite images, two models, and the body force: i) northern Okinawa trough, ii) western Fukue Island, iii) southwestern Jeju Island, and iv) near the IORS. With KdV model and empirical model established and thus the ability to determine the propagation time to any location in the region of interest, the empirical model can serve as the basis for a prediction system.

Groups of NLIWs were predominantly observed in the SAVEX15 area during, or a couple of days after, spring tides, with time intervals departing from the canonical semidiurnal period (M2). Among the sites of potential generation of semidiurnal internal tides in the ECS, addressed by depth-integrated, internal tide-generating body force, ii) western Fukue Island is the most likely source of the NLIWs observed in the SAVEX15 area, accounting for the time intervals that depart from the M2 period and the southwestward propagation direction of NLIWs.

This study is the first to report the characteristics of spring NLIWs based on moored and underway observations, and the first to identify potential generation sites in the northern ECS. Characterizing the seasonal cycles of propagating speed of NLIWs is an important first step toward a better understanding of and reliably predicting NLIWs in the northeastern ECS, and will allow to better design a comprehensive field experiment in the future.

References

- Akima, H. (1970). A new method of interpolation and smooth curve fitting. *J. ACM* 17, 589–602.
- Alford, M. H. (2003). Redistribution of energy available for ocean mixing by long-range propagation of internal waves. *Nature* 423, 159–162. doi:10.1038/nature01628.
- Alford, M.H.; Lien, R.-C.; Simmons, H.; Klymak, J.; Ramp, S.; Yang, Y.-J.; Tang, D.; Chang, M.-H. Speed and Evolution of Nonlinear Internal Waves Transiting the South China Sea. *J. Phys. Oceanogr.* 2010, 40, 1338–1355, <https://doi.org/10.1175/2010jpo4388.1>.
- Alford, M. H., Peacock, T., Mackinnon, J. A., Nash, J. D., Buijsman, M. C., Centuroni, L. R., et al. (2015). The formation and fate of internal waves in the South China Sea. *Nature* 521, 65–69. doi:10.1038/nature14399.
- Alpers, W., He, M. X., Zeng, K., Quo, L. F., and Li, X. M. (2005). The distribution of internal waves in the East China Sea and the Yellow Sea studied by multi-sensor satellite images. *Int. Geosci. Remote Sens. Symp.* 7, 4784–4787. doi:10.1109/IGARSS.2005.1526742.
- Apel, J. R., Ostrovsky, L. A., Stepanyants, Y. A., and Lynch, J. F. (2007). Internal solitons in the ocean and their effect on underwater sound. *J. Acoust. Soc. Am.* 121, 695–722. doi:10.1121/1.2395914.
- Apel, J. R., and Jackson, C. (2003). A new analytical model for internal solitons in the ocean. *J. Phys. Oceanogr.* 33, 2247–2269. doi:10.1175/1520-0485(2003)033<2247:ANAMFI>2.0.CO;2.
- Bai, X., Liu, Z., Zheng, Q., Hu, J., Lamb, K. G., and Cai, S. (2019). Fission of Shoaling Internal Waves on the Northeastern Shelf of the South China Sea. *J. Geophys. Res. Ocean.* 124, 4529–4545. doi:10.1029/2018JC014437.
- Baines, P. G. (1982). On internal tide generation models. *Deep Sea Res. Part A, Oceanogr. Res. Pap.* 29, 307–338. doi:10.1016/0198-0149(82)90098-X.
- Boegman, L., and Stastna, M. (2019). Sediment resuspension and transport by internal solitary waves. *Annu. Rev. Fluid Mech.* 51, 129–154. doi:10.1146/annurev-fluid-122316-045049.
- Bogucki, D.; Dickey, T.; Redekopp, L. G. (1997). Sediment resuspension and transport by Sediment Resuspension and Mixing by Resonantly Generated Internal Solitary Waves solitary waves. *J. Phys. Oceanogr.* 27, 1181–1196. doi:10.1146/annurev-fluid-122316-045049.
- Byun, G.; Song, H.C. Adaptive array invariant. *J. Acoust. Soc. Am.* 2020, 148, 925–933, <https://doi.org/10.1121/10.0001768>.
- Chang, M.-H.; Lien, R.-C.; Yang, Y.J.; Tang, T.Y. Nonlinear Internal Wave Properties Estimated with Moored ADCP Measurements. *J. Atmos. Ocean. Technol.* 2011, 28, 802–815, <https://doi.org/10.1175/2010jtecho814.1>.
- Cai, S.; Xie, J.; Xu, J.; Wang, N.; Chen, Z.; Deng, X.; Long, X. Monthly variation of

- some parameters about internal solitary waves in the South China sea. *Deep Sea Res. Part I Oceanogr. Res. Pap.* 2013, 84, 73–85, <https://doi.org/10.1016/j.dsr.2013.10.008>.
- Craig, W.; Guyenne, P.; Sulem, C. The surface signature of internal waves. *J. Fluid Mech.* 2012, 710, 277–303, <https://doi.org/10.1017/jfm.2012.364>.
- Cho, C., Nam, S., and Song, H. (2016). Seasonal variation of speed and width from kinematic parameters of mode-1 nonlinear internal waves in the northeastern East China Sea. *J. Geophys. Res. Oceans.* 121, 5942–5958. doi:10.1002/2016jc012035.
- D’Asaro, E. A., Lien, R. C., and Henyey, F. (2007). High-frequency internal waves on the Oregon continental shelf. *J. Phys. Oceanogr.* 37, 1956–1967. doi:10.1175/JPO3096.1.
- Drake, D.E.; Cacchione, D.A. Field observations of bed shear stress and sediment resuspension on continental shelves, Alaska and California. *Cont. Shelf Res.* 1986, 6, 415–429, [https://doi.org/10.1016/0278-4343\(86\)90081-6](https://doi.org/10.1016/0278-4343(86)90081-6).
- Egbert, G. D., and Erofeeva, S. Y. (2002). Efficient inverse modeling of barotropic ocean tides. *J. Atmos. Ocean. Technol.* 19, 183–204. doi:10.1175/1520-0426(2002)019<0183:EIMOBO>2.0.CO;2.
- Greskowiak, J. Tide-induced salt-fingering flow during submarine groundwater discharge. *Geophys. Res. Lett.* 2014, 41, 6413–6419, <https://doi.org/10.1002/2014gl061184>.
- Grimshaw, R., Wang, C., and Li, L. (2016). Modelling of polarity change in a nonlinear internal wave train in Laoshan Bay. *J. Phys. Oceanogr.* 46, 965–974. doi:10.1175/JPO-D-15-0136.1.
- Ha, K. J., Nam, S., Jeong, J. Y., Moon, I. J., Lee, M., Yun, J., et al. (2019). Observations utilizing Korea ocean research stations and their applications for process studies. *Bull. Am. Meteorol. Soc.* 100, 2061–2075. doi:10.1175/BAMS-D-18-0305.1.
- Helfrich, K.R.; Melville, W.K. Long Nonlinear Internal Waves. *Annu. Rev. Fluid Mech.* 2006, 38, 395–425, <https://doi.org/10.1146/annurev.fluid.38.050304.092129>.
- Hsu, M. K., Liu, A. K., and Liu, C. (2000). A study of internal waves in the China Seas and Yellow Sea using SAR. *Cont. Shelf Res.* 20, 389–410. doi:10.1016/S0278-4343(99)00078-3.
- Jackson, C. (2007). Internal wave detection using the Moderate Resolution Imaging Spectroradiometer (MODIS). *J. Geophys. Res. Ocean.* 112, 1–13. doi:10.1029/2007JC004220.
- Jackson, C.R. (2009). An empirical model for estimating the geographic location of nonlinear internal solitary waves. *J. Atmos. Ocean. Technol.* 26, 2243–2255. doi:10.1175/2009JTECHO638.1.
- Jackson, C.R., da Silva, J.C.B., and Jeans, G. (2012). The generation of nonlinear internal waves. *Oceanography.* 25(2):108–123. doi: 10.5670/oceanog.2012.46.

- Karang, I.W.G.A.; Chonnaniyah; Osawa, T. Internal solitary wave observations in the Flores Sea using the Himawari-8 geostationary satellite. *Int. J. Remote. Sens.* 2019, 41, 5726–5742, <https://doi.org/10.1080/01431161.2019.1693079>.
- Kinsler, L.E.; Frey, A.R.; Coppens, A.B.; Sanders, J.V. *Fundamentals of Acoustics*; John Wiley & Sons: Hoboken, NJ, USA, 1999.
- Klymak, J. M., and Moum, J. N. (2003). Internal solitary waves of elevation advancing on a shoaling shelf. *Geophys. Res. Lett.* 30, 8–11. doi:10.1029/2003GL017706.
- Korteweg, D. J., and de Vries, G. (1895). XLI. On the change of form of long waves advancing in a rectangular canal, and on a new type of long stationary waves. *London, Edinburgh, Dublin Philos. Mag. J. Sci.* 39, 422–443. doi:10.1080/14786449508620739.
- Kuperman, W. A.; Lynch, J. F. (2004). Shallow-Water Acoustics. *Phys. Today* 57, 55–61. doi:10.1016/B978-0-12-811240-3.00007-2.
- Lee, O.S. OBSERVATIONS ON INTERNAL WAVES IN SHALLOW WATER. *Limnol. Oceanogr.* 1961, 6, 312–321, <https://doi.org/10.4319/lo.1961.6.3.0312>.
- Lee, S.-W., Nam, S., and Song, H. (2020) Moored and ship-based oceanographic data collected during Shallow-water Acoustic Variability EXperiment (SAVEX15). SEANO, doi:10.17882/72285.
- Lee, S.-W., and Nam, S. (2021). Estimation of Propagation Speed and Direction of Nonlinear Internal Waves from Underway and Moored Measurements. *J. Mar. Sci. Eng.* 9, 1089. Doi: 10.3390/jmse9101089
- Lee, J. H.; Lozovatsky, I.; Jang, S.-T.; Jang, C. J.; Hong, C. S.; Fernando, H. J. S. (2006). Episodes of nonlinear internal wave in the northern East China Sea. *Geophys. Res. Lett.* 33, 2–6. doi:10.1029/2006GL027136.
- Li, X., Zhao, Z., and Pichel, W. G. (2008). Internal solitary waves in the northwestern South China Sea inferred from satellite images. *Geophys. Res. Lett.* 35, 1–7. doi:10.1029/2008GL034272.
- Li, D., Chou, W. C., Shih, Y. Y., Chen, G. Y., Chang, Y., Chow, C. H., et al. (2018). Elevated particulate organic carbon export flux induced by internal waves in the oligotrophic northern South China Sea. *Sci. Rep.* 8, 1–7. doi:10.1038/s41598-018-20184-9.
- Lindsey, D.T.; Nam, S.; Miller, S.D. Tracking oceanic nonlinear internal waves in the Indonesian seas from geostationary orbit. *Remote. Sens. Environ.* 2018, 208, 202–209, <https://doi.org/10.1016/j.rse.2018.02.018>.
- Liu, A. K., Chang, Y. S., Hsu, M. K., & Liang, N. K. (1998). Evolution of nonlinear internal waves in the East and South China Seas. *Journal of Geophysical Research: Oceans*, 103(C4), 7995-8008.
- Locarnini, R.A., Mishonov, A.V., Baranova, O.K., Boyer, T.P., Zweng, M.M., Garcia, H.E., Reagan J.R., Seidov, D., Weathers, K.W., Paver, C.R., and Smolyar, I.V. (2019). *World Ocean Atlas 2018, Volume 1: Temperature*. A. Mishonov, Technical Editor. NOAA Atlas NESDIS 81. 52pp. doi: <http://www.nodc.noaa.gov/OC5/indprod.html>.

- Lozovatsky, I., Jinadasa, P., Lee, J. H., and Fernando, H. J. (2015). Internal waves in a summer pycnocline of the East China Sea. *Ocean Dyn.* 65, 1051–1061. doi:10.1007/s10236-015-0858-2.
- Lucas, A. J., Franks, P. J. S., and Dupont, C. L. (2011). Horizontal internal-tide fluxes support elevated phytoplankton productivity over the inner continental shelf. *Limnol. Oceanogr. Fluids Environ.* 1, 56–74. doi:10.1215/21573698-1258185.
- Lynch, J.; Newhall, A. *Shallow-Water Acoustics.* 2017, 403–467, <https://doi.org/10.1016/b978-0-12-811240-3.00007-2>.
- MacKinnon, J. A., and Gregg, M. C. (2003). Mixing on the late-summer new England shelf-Solibores, shear, and stratification. *J. Phys. Oceanogr.* 33, 1476–1492. doi:10.1175/1520-0485(2003)033<1476:MOTLNE>2.0.CO;2.
- McSweeney, J.; Lerczak, J.A.; Barth, J.A.; Becherer, J.; Colosi, J.A.; MacKinnon, J.A.; MacMahan, J.H.; Moum, J.N.; Pierce, S.D.; Waterhouse, A.F. Observations of Shoaling Nonlinear Internal Bores across the Central California Inner Shelf. *J. Phys. Oceanogr.* 2020, 50, 111–132, <https://doi.org/10.1175/jpo-d-19-0125.1>.
- Mirshak, R.; Kelley, D.E. Inferring Propagation Direction of Nonlinear Internal Waves in a Vertically Sheared Background Flow. *J. Atmos. Ocean. Technol.* 2009, 26, 615–625, <https://doi.org/10.1175/2008jtecho632.1>.
- Moum, J.N.; Smyth, W.D. The pressure disturbance of a nonlinear internal wave train. *J. Fluid Mech.* 2006, 558, 153–177, <https://doi.org/10.1017/s0022112006000036>.
- Moum, J. N., Farmer, D. M., Shroyer, E. L., Smyth, W. D., and Armi, L. (2007). Dissipative losses in nonlinear internal waves propagating across the continental shelf. *J. Phys. Oceanogr.* 37, 1989–1995. doi:10.1175/JPO3091.1.
- Moum, J.N.; Nash, J.D. Seafloor Pressure Measurements of Nonlinear Internal Waves. *J. Phys. Oceanogr.* 2008, 38, 481–491, <https://doi.org/10.1175/2007jpo3736.1>.
- Muacho, S., Da Silva, J. C. B., Brotas, V., and Oliveira, P. B. (2013). Effect of internal waves on near-surface chlorophyll concentration and primary production in the Nazaré Canyon (west of the Iberian Peninsula). *Deep. Res. Part I Oceanogr. Res. Pap.* 81, 89–96. doi:10.1016/j.dsr.2013.07.012.
- Nam, S. H., Kim, D. J., Lee, S. W., Kim, B. G., Kang, K. M., and Cho, Y. K. (2018). Nonlinear internal wave spirals in the northern East China Sea. *Sci. Rep.* 8, 1–9. doi:10.1038/s41598-018-21461-3.
- Niwa, Y., and Hibiya, T. (2004). Three-dimensional numerical simulation of M2 internal tides in the East China Sea. *J. Geophys. Res. C Ocean.* 109, 1–14. doi:10.1029/2003JC001923.
- Park, J.; Seong, W.; Yang, H.; Nam, S.; Lee, S.-W. Array tilt effect induced by tidal currents in the northeastern East China Sea. *Ocean. Eng.* 2019, 194, 106654, <https://doi.org/10.1016/j.oceaneng.2019.106654>.
- Park, J.; Seong, W.; Yang, H.; Nam, S.; Lee, S.-W.; Choo, Y. Broadband acoustic signal variability induced by internal solitary waves and semidiurnal internal

- tides in the northeastern East China Sea. *J. Acoust. Soc. Am.* 2019, 146, 1110–1123, <https://doi.org/10.1121/1.5121715>.
- Pineda, J. (1991). Predictable upwelling and the shoreward transport of planktonic larvae by internal tidal bores. *Science*. 253, 548–551. doi:10.1126/science.253.5019.548.
- Ramp, S.; Tang, T.Y.; Duda, T.; Lynch, J.; Liu, A.; Chiu, C.-S.; Bahr, F.; Kim, H.-R.; Yang, Y.-J. Internal Solitons in the Northeastern South China Sea Part I: Sources and Deep Water Propagation. *IEEE J. Ocean. Eng.* 2004, 29, 1157–1181, <https://doi.org/10.1109/joe.2004.840839>.
- Scotti, A.; Butman, B.; Beardsley, R.C.; Alexander, P.S.; Anderson, S. A Modified Beam-to-Earth Transformation to Measure Short-Wavelength Internal Waves with an Acoustic Doppler Current Profiler. *J. Atmos. Ocean. Technol.* 2005, 22, 583–591, <https://doi.org/10.1175/jtech1731.1>.
- Scotti, A., and Pineda, J. (2007). Plankton accumulation and transport in propagating nonlinear internal fronts. *J. Mar. Res.* 65, 117–145. doi:10.1357/002224007780388702.
- Sea-Bird Electronics Inc. (2005). SEASOFT-Win32: SBE Data Processing, CTD data processing and plotting software for windows 95/98/NT/2000/XP, software release 5.34a and later, Sea-Bird Electronics Inc., Bellevue, Washington, USA, 124 pp.
- Shen, H., Perrie, W., and Johnson, C. L. (2020). Predicting Internal Solitary Waves in the Gulf of Maine. *J. Geophys. Res. Ocean.* 125. doi:10.1029/2019JC015941.
- Shroyer, E. L., Moum, J. N., and Nash, J. D. (2010). Vertical heat flux and lateral mass transport in nonlinear internal waves. *Geophys. Res. Lett.* 37, 1–5. doi:10.1029/2010GL042715.
- Shroyer, E.L.; Moum, J.N.; Nash, J. Observations of Polarity Reversal in Shoaling Nonlinear Internal Waves. *J. Phys. Oceanogr.* 2009, 39, 691–701, <https://doi.org/10.1175/2008jpo3953.1>.
- Smith, C. M., and Bradley, D. L. (2010). Effects of propagating internal waves on shallow-water acoustic propagation during the transverse acoustic variability experiment of 2008.
- Song, H., Cho, C., Hodgkiss, W., Nam, S. H., Kim, S. M., and Kim, B. N. (2018). Underwater sound channel in the northeastern East China Sea. *Ocean Eng.* 147, 370–374. doi:10.1016/j.oceaneng.2017.10.045.
- Teixeira, M., Warn-Varnas, A., Apel, J., and Hawkins, J. (2006). Analytical and observational studies of internal solitary waves in the Yellow Sea. *J. Coast. Res.* 22, 1403–1416. doi:10.2112/04-0339.1.
- Tensubam, C.M.; Raju, N.J.; Dash, M.K.; Barskar, H. Estimation of internal solitary wave propagation speed in the Andaman Sea using multi-satellite images. *Remote. Sens. Environ.* 2020, 252, 112123, <https://doi.org/10.1016/j.rse.2020.112123>.
- Ullman, D. S., and Hebert, D. (2014). Processing of underway CTD data. *J. Atmos. Ocean. Technol.* 31, 984–998. doi:10.1175/JTECH-D-13-00200.1.

- Villamaña, M., Mouriño-Carballido, B., Marañón, E., Cermeño, P., Chouciño, P., da Silva, J. C. B., et al. (2017). Role of internal waves on mixing, nutrient supply and phytoplankton community structure during spring and neap tides in the upwelling ecosystem of Ría de Vigo (NW Iberian Peninsula). *Limnol. Oceanogr.* 62, 1014–1030. doi:10.1002/lno.10482.
- Wang, J., Huang, W., Yang, J., Zhang, H., and Zheng, G. (2013). Study of the propagation direction of the internal waves in the South China Sea using satellite images. *Acta Oceanol. Sin.* 32, 42–50. doi:10.1007/s13131-013-0312-6.
- Whalen, C. B., de Lavergne, C., Naveira Garabato, A. C., Klymak, J. M., MacKinnon, J. A., and Sheen, K. L. (2020). Internal wave-driven mixing: governing processes and consequences for climate. *Nat. Rev. Earth Environ.* 1, 606–621. doi:10.1038/s43017-020-0097-z.
- Yoon, S.; Yang, H.; Seong, W. Deep learning-based high-frequency source depth estimation using a single sensor. *J. Acoust. Soc. Am.* 2021, 149, 1454–1465, <https://doi.org/10.1121/10.0003603>.
- Zhang, S.; Alford, M.H.; Mickett, J.B. Characteristics, generation and mass transport of nonlinear internal waves on the Washington continental shelf. *J. Geophys. Res. Oceans* 2015, 120, 741–758, <https://doi.org/10.1002/2014jc010393>.
- Zhao, Z., Klemas, V., Zheng, Q., Li, X., and Yan, X. H. (2004). Estimating parameters of a two-layer stratified ocean from polarity conversion of internal solitary waves observed in satellite SAR images. *Remote Sens. Environ.* 92, 276–287. doi:10.1016/j.rse.2004.05.014.
- Zweng, M.M, Reagan, J.R., Seidov, D., Boyer, T.P., Locarnini, R.A., Garcia, H.E., Mishonov, A.V., Baranova, O.K., Weathers, K.W., Paver, C.R., and Smolyar, I.V. (2019). *World Ocean Atlas 2018, Volume 2: Salinity*. A. Mishonov, Technical Editor, NOAA Atlas NESDIS 82, 50pp. doi: <http://www.nodc.noaa.gov/OC5/indprod.html>

Abstract in Korean

해양 비선형 단주기(관성주기보다 부력주기에 더 근접한 주기) 내부파(oceanic nonlinear internal waves)는 전 세계 곳곳의 성층화된 해양에서 빈번하게 발생하고, 열, 에너지, 물질 수송 및 재분배에 중요한 역할을 한다. 해양 내부파로 인한 난류 혼합과 수층구조의 변동은 해양 생태계 교란, 어장 형성 및 수중음향 신호의 굴절/반사/산란 등에 지대한 영향을 미치고, 해양 내부파와 해표면 파랑은 상호 작용하여 다양한 환경변화를 유발하는 것으로 알려져 있다. 비선형 단주기 내부파와 그 영향들을 이해하기 위해서는 비선형 단주기 내부파를 관측하고, 그 특성을 파악해야 한다. 또한, 비선형 단주기 내부파의 생성과 그 전파 과정의 이해가 중요하다. 본 연구에서는 동중국해 북부 해역에서 2015년 5월에 현장 관측 승선 조사를 통해 관측된 비선형 단주기 내부파의 특성을 파악하기 위해 비선형 단주기 내부파의 전파 방향과 속도를 추정하는 방법을 제시하고, 관측된 비선형 단주기 내부파의 특성, 생성, 전파를 규명하였다.

현장 관측 승선 조사에서 수집된 이동형 관측과 계류 관측을 통해 비선형 단주기 내부파의 전파 속도와 전파 방향을 추정하였다. 도플러 이동 방법(Doppler Shift method)은 이동하는 선박(관측장비)으로부터 비선형 단주기 내부파의 상대적 거리 변화에 의해 유도된 도플러 이동을 사용하여 내부파의 전파 방향을 추정한다. 시간 차이 방법(Time lag method)은 서로 다른 시간에 다른 위치에서 관측된 동일한 비선형 단주기 내부파를 두 위치의 거리와 시간 차이를 사용하여 내부파의 전파 방향을 추정한다. 두 방법으로부터 비선형 단주기 내부파의 방향과 속도를 최적화하기 위해서는 두 가지 방법에 의해 독립적으로 추정된 전파 방향의 차이를 최소화해야 한다. 이 방법은 2015년 5월과 2018년 8월에 동중국해 북부해역에서 관측된 두 가지 승선 조사 사례에 적용하였다. 추정된 전파 속도는 2015년 5월에는 0.05 m/s 이하의 차이로 이론적 전파속도와 잘 일치하였고, 2018년 8월에는 0.25m/s의 차이를 보이며 이론적 전파속도와 일치하지 않았지만, 이러한 결과는 2006년 결과와 일치하며 이론적 결과의 한계를 보여주었다. 추정된 전

과 방향을 인공위성에서 관측된 비선형 단주기 내부파와 비교한 결과 남서향의 전파로 잘 일치하였다. 이 연구는 동중국해 북부해역과 같이 넓은 대륙붕에서 비선형 단주기 내부파의 전파 속도와 방향을 현장 관측 승선 조사를 통해 추정하는 데 의의가 있다.

2015년 5월 14-28일 기간 동안 동중국해 북부해역에서 수집된 2기의 계류 관측 수온 시계열 자료, 1,064회의 UCTD 및 26회의 표준 CTD 프로파일링 관측 수온과 염분 자료를 분석하고, 2015년부터 2019년까지 동중국해 북부해역에서 수집된 MODIS 위성 영상과 국립수산과학원 정선관측을 통해 지난 40년간(1980-2019년) 동중국해 북부해역에서 수집한 표준 수심의 수온과 염분 자료를 분석하여, 봄철 비선형 단주기 내부파 특성을 규명하고 그 생성 및 전파 과정을 토의하였다. 관측된 비선형 단주기 내부파는 4~16 m의 진폭, 380~600 m의 특성폭, 0.64~0.72 m/s의 전파 속도로 남서쪽 방향으로 전파하였다. 비선형 단주기 내부파는 대조기 기간 또는 그 이후 며칠 동안 관측되었고, M2 조석 주기보다 24-96분 짧은 시간 간격으로 관측되었다. 2015년부터 2019년간의 93장의 인공위성 영상을 통해 최소 3개의 잠재적 생성지를 추정하고 내부 조석 힘으로부터 4개의 잠재적 생성지와 비교하였다. 이층 유체를 가정한 KdV 모델에 관측된 봄철 성층 조건을 적용하고, 수심의 함수로 전파속도를 추정하는 경험 모델의 결과와 비교하여 수심과 성층에 따라 증가하는 전파속도를 확인하였다. 이 경험 모델을 동중국해 북부 해역에 적용하여 잠재적인 4개의 생성 해역으로부터 관측 해역으로의 내부파 전파를 분석한 결과, 후쿠시마 서부에서 생성되어 남서향 전파하며 관측해역에 도달하는 것으로 모의되었다. 본 연구는 동중국해 북부해역 봄철 비선형 단주기 내부파의 특성과 그 생성 및 전파 과정에 대한 이해도를 높여 궁극적으로 해수 및 생지화학적 순환, 수직 혼합, 수중 음전달에 중요한 시사점을 가진다.

이 연구는 동중국해 북부해역에서 비선형 단주기 내부파를 처음으로 5월에 관측하여 특성화한 연구이며, 기존에 알려지지 않은 내부파 생성지와 전파를 포함하여 4개의 내부파의 생성지를 밝힌 것에 그 의의를 찾을 수 있다.